國立台灣大學生物環境系統工程學研究所

碩士論文

Graduate Institute of Bioenvironmental Systems Engineering

National Taiwan University

Master Thesis

以二維有限元素形貌動力模式探討渠道強制效應對自由沙洲之影響

Investigating the Influences of Channel Forcing Effect on Free Bars Using a 2D Finite-Element Morphodynamic Model

邵允銓

Yun-Chuan Shao

指導教授：吳富春 Fu-Chun Wu 教授

中華民國九十七年六月

June 2008

國立台灣大學

生物環境系統工程研究所

邵允銓　　君之碩士論文

經考試合格特此證明

學位考試委員　　顏清連 顏清連

楊德良 楊德良

卡艾瑋 Hans Gaerl

指導教授　　吳富春 吳富春

所長　　黃宏斌 黃宏斌

中華民國九十七年六月

謝誌

研究所求學的日子裡衷心地感謝吳富春老師的諄諄教誨，引領我走入學術的殿堂，開拓了我的視野與想法，不僅在學術研究上給與莫大的支持與指導，在生活與待人處事的細節上亦受惠老師良多，研究所雖僅短短數年，但受吳老師教化所學的是一生受用的。感謝卡艾瑋老師總是大方地的分享研究經驗與成果，讓我在實驗的技術與執行上更加的靈活，希望能把論文與卡老師分享是驅使我以英文撰寫原動力之一。感謝顏清連老師在數值模擬與物理意義之間討論給與我許多寶貴的意見，使我的論文更為的完整。感謝楊德良老師對於數值方法上的建議與指導讓我對數值領域有更深的興趣與探索。

生活在研究室的日子裡，要特別感謝陳嘉欣小姐替我們處理許多庶務，為我們分憂解勞，讓我們無後顧之憂的專心在研究上。感謝葉子豪學長、陳臻琪學長幫我解決了無數的大大小小的問題。謝謝潘泰斗、顧尚真、林鈺翔、陳昱辰等眾多學弟一起分攤研究室的人力工作。感謝助理石武融、李依珊、吳子青一起為研究室分憂解勞。感謝卡老師門下賴悅仁學長、柯文韜學長、粟群超、紀泰安、許珮蓁同學大方分享研究設備與上課筆記，與你們互相學習交流讓我學到很多。謝謝黃國文技師與水工所翁總管於流力實驗與水槽實驗上的幫忙，特別感謝莊詔傑學長與何嵩晟學長分享許多人生的歷練與經驗，讓我於人生的路上有更明確的目標。

感謝許兄中駿、謝兄清智、甘兄智仁、許兄詩涵、王兄翔生、范兄振國、塗兄宗杰、塗氏俞慧、周兄宏泰還有郁潔老師，陪我一起互相打氣，打打鬧鬧的撐過許多日子，還多了一個乾女兒范家甄，有你們真好！感協羅多倫台大分店的大姐們總是讓我的早餐與晚餐 VIP 升級，讓我能有更充足的補給。

最後要特別感謝我的家人對我的包容與支持，讓可以全心全意的把心思放在學校，謝謝你們的付出與犧牲。

Contents

Chap 3 Model Validation

Chap 4 Forcing Effect of Width Variation on Free Bars

Chap 5 Conclusions

摘　要

本研究利用二維有限元素河川形貌動力模式，探討自由沙洲受變寬渠強制效應之影響。本研究所發展數值模式具有兩個特色：第一是使用流線曲率項來修正底床拖移載受到水流二次流影響後的運動方向。第二是以流線上風演算法處理泥沙連續方程式，使數值模式具有模擬強制沙洲(兩側沙洲、中央沙洲)與自由沙洲共存之能力。數值模擬發現強制沙洲與自由沙洲共存狀態屬於疊加，因此可將自由沙洲之演變取出討論。研究結果顯示自由沙洲之發展到達平衡狀態時，其波高、波長與波速受到渠寬變化所影響，會產生穩定的周期性波動，其週期平均值會隨變寬渠之振幅與波數增大而減小，本研究進一步將變寬渠之振幅與波數整合為一強制因子，對自由沙洲之影響效應進行量化分析，證明自由沙洲會受渠寬變化影響而被壓抑。

關鍵字：形貌動力模式、有限元素法、流線上風演算法、自由沙洲、強制效應。

Abstract

In this study a two-dimensional finite-element (2D FE) morphodynamic model is developed to investigate the forcing effects of periodic width variation on free bars. Two features of the proposed model include: (1) The streamline curvature are used to correct the bed load direction effected by secondary flows. (2) The streamline upwind Petrov-Galerkin (SUPG) scheme is applied to solve the sediment continuity equation, which makes it possible to simulate the coexistence of free bars and forced bars (such as side bars and central bars). It is found that the coexistence of free and forced bars is a superposition of the two types of bedform. Thus the free-bar component can be extracted for our study. The results reveal that the bar height, wavelength and celerity of free bars affected by the effect of width variation lead to a periodic wavy pattern when the development of free bars reach the equilibrium state. The mean components of free bars in a cycle of channels with variable-width are inverse proportioned to the amplitude and wave number of width variation. We further derive a forcing factor by combining the amplitude with wave number of width variation and quantitatively prove that the free bars are suppressed by the forcing factor of channels with variable width.

Keywords: Morphodynamic model, finite-element method, streamline-upwind Patrov-Galerkin method, free bars, forcing effect.

List of Tables

List of Figures

List of Symbols

$\mathrm{A_c}$	dimensionless amplitude of width variation
A_e	element area
$\left(\mathrm{A}_x, \mathrm{A}_y\right)$	the advection matrices in the (x, y) directions
B^*	channel half-width
B_0	mean half-width
b_0	channel wall perturbation
C_f	the bed friction coefficient
C_s	dimensionless local curvature of streamline
D_{sm}	average grain size of sediment
$\mathrm{d_s}$	grain size
D_w	flow depth (m)
Fr	Froude number
$\left(\mathrm{f}_x, \mathrm{f}_y\right)$	the flux vectors in the (x, y) directions
K_s	the roughness height
N_i	the shape function of node i
N_i	a diagonal matrix of N_i

$\hat{\mathrm{N}}_i$	the weighting function matrix of node i
(n_x, n_y)	(x, y) component of outward vector normal to the boundary element
P	the pressure
Q_b	sediment transport discharge
(Q_{bx}, Q_{by})	sediment transport in the (x, y) directions
Q_n	the fluid flux across the boundary segment
(Q_x, Q_y)	unit discharge in the (x, y) directions
q_0	the unit discharge imposed in boundary segment
$\overline{R}_{ij}$	the vertically averaged Reynolds stress
r	an empirical coefficient
S_0	slope of channel
S_t	the source vector
U_*	the shear velocity
(U, V, W)	the velocities in the (x, y, z) directions
(U_0, V_0)	the depth average velocity components
V_h	the vertically averaged eddy viscosities in the horizontal direction

(W_x, W_y)	the upwind matrices applied to flow in the (x, y) directions
$(W_{z_b,x}, W_{z_b,y})$	the upwind matrices applied to sediment continuity equation
z_b	bed elevation
α	angle between the sediment trajectory and x-direction
β	ratio of mean half-width to reference flow depth
χ	angle between the local bed shear stress and x-direction
Φ	bed load intensity
Γ_e	the segment of the boundary element
φ	the solution of the governing equation
$\tilde{\varphi}$	the approximate solution of the element
η	bed elevation
λ_b	dimensionless wave number of width variation
λ_c	wavelength of channels with variation width
λ_p	bed porosity
θ	Shields stress
θ_c	dimensionless critical shear stress
ρ	density of fluid
ρ_s	density of sediment

(τ_x, τ_x)	bed shear stress in the (x, y) directions
Ω_e	an element domain
ω	an upwind coefficient
ζ_i	the solution of node i

Chapter 1 Introduction

1.1 Statement of Problem

The evolution processes of bed configuration in the alluvial rivers are abundant and complicated. The bedform of natural rivers may be generated by the forcing effect of the channel geometry, e.g., width variation and curvature, and any disturbances that trigger free deformation on the riverbed. The former may yield the stationary forced bar formation and the latter may induce the free migrating alternate bars, as shown in Figure 1-1. In natural rivers, forced and free bars often coexist and interact with each other. The flowfield and morphology of a river are unsteady and dynamic, and thus affect river management issues such as channel training, flood defense, riverine habitat conservation/restoration, and transport of pollutants. In order to accurately predict the evolution of dynamic bedform in natural channels, a better understanding of the influences of these forcing effects on free migrating alternate bars is necessary. The aims of this study are to develop a two-dimensional (2D) finite element (FE) morphodynamic model and systematically investigate these problems. The results of this study may provide useful information guiding more dynamic and comprehensive practices of river engineering.

(a)

(b)

Figure 1-1 (a) Free alternate bars in Shi-hu Creek, Taiwan; (b) Central bars in Tai-ping Creek, Taiwan.

1.2 Literature Review

In natural rivers bars are a kind of general large-scale bed topography which the bar height and wavelength are of the order of the flow depth and the channel width, respectively. According to the geometry, kinematic characteristics and emergence location in the channel, bars are grouped into free and forced bars. It is now well established that bars formation can be explained as the results of an instability mechanism which come from the channel geometry nonuniformities or the perturbation on the planimetric river bed configuration. Recent studies of free and forced bars are described as follows.

1.2.1 Study of free bars

Free bars migrating downstream in a straight channel belong to an instability mechanism induced by the spontaneous perturbation on the planimetric erodible bed and are characterized by a sequence of steep consecutive diagonal fronts with deep pools at the lee face and gentler riffles along the stoss face. Figure 1-2 displays a top view of the free bars which are so called alternate bars due to the diagonal front across the transverse direction. Experimental observations support the perturbation on the river bed perturbs flow and trigger a series of bar formation downstream [Fujita and Muramoto, 1985; Garcia and Nino, 1993; Lanzoni, 2001].

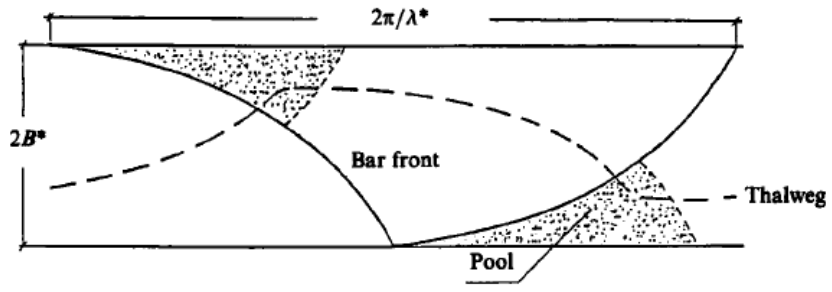

Figure 1-2 Sketch of alternate-bar structure. [Colombini et al., 1987]

In the early stage of studies of free bars, linear instability theory offered a convenient tool to investigate a selection of the most unstable wavelength promoting free bars to develop [Callander, 1969; Engelund and Skovgaard, 1973; Parker, 1976; Fredsoe, 1978; Blondeaux and Seminara, 1985; Nelson and Smith, 1989; Lanzoni, 2000]. Figure 1-3 shows the representative result of the linear theory, the solid line represent the neutral state at which the growth rate of perturbation are eliminated and distinguish the stable and unstable conditions to judge the developing of free bars. The shortcoming of linear theory appears when the width-to-depth ratio becomes significantly large because the nonlinear terms become more important. The nonlinear interaction between finite amplitude disturbances of different wavelength of free bars may not be ignored. As an overall trend, linear theory underpredicts bar wavelength and overpredicted the bar celerity.

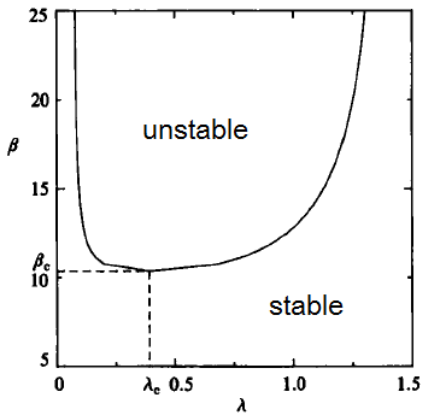

Figure 1-3 A typical neutral curve for alternate bar formation. [Colombini et al., 1987]

The weakly nonlinear theory developed in the neighborhood of critical conditions has been applied to derive the finite amplitude equation for the marginally unstable bed forms. The Landau equation derived by Colombini et al. (1987) and Fukuoka (1989) have an ability to capture the long-term behavior of a single unstable wave. Schielen et al. (1993) based on the Landau equation to obtain the

Ginzburg-Landau equation that has the ability to capture the evolution of the envelope amplitude of the wave group. The weakly nonlinear theory improves the prediction of equilibrium bar height, but not wavelength and celerity, due to that the weakly nonlinear theory does not account for the modifying of wavelength of the perturbation when the free bars are developing.

The numerical approach applied to the fully nonlinear perturbation had been proposed in the literature [Nelson and Smith, 1989; Colombini and Tubino, 1991; Defina, 2003; Bernini et al., 2006]. The perturbations are given artificially in time and space trigging bar formation in the numerical simulation. The process of bar evolution in the numerical simulation is similar to the experiment observation [Lanzoni, 2001]. A fully nonlinear numerical model has the ability to describe the nonlinear interaction between free bars in the evolution process in an infinite straight channel. The equilibrium bar height, wavelength and celerity are strictly related to one another regardless of the type of initial perturbation [Difina, 2003]. Figure 1-4 shows the main result of Defina's numerical experiments, where the bar height and wavelength are inversing proportional to the celerity in the equilibrium.

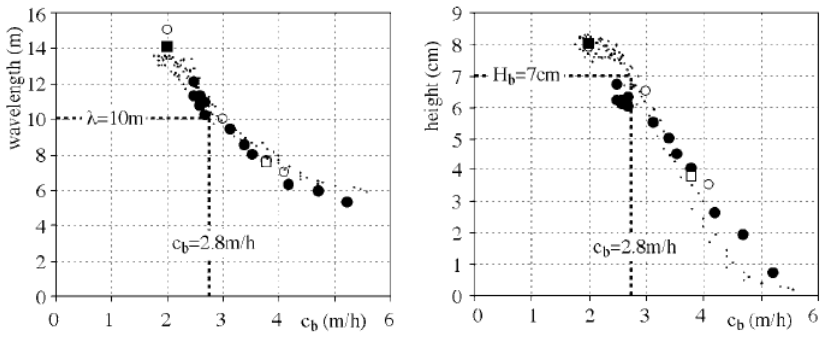

Figure 1-4 Free bars wavelength and height as a function of bar celerity in Defina's numerical experiments. [Defina, 2003]

1.2.2 Study of forced bars

The channel curvature and width variation are two types of channel geometry nonuniformities that generate the forced bars. The channel curvature induced point bars had been widely studied in the literature [Ikeda and Nishimura, 1985; Blondeaux and Seminara, 1985; Seminara and Tubino, 1989; Parker and Johannesson, 1989; Whiting and Dietrich, 1993; Seminara et al., 2001].

The aim of our study is focused on the channels with variable width. According to the transverse bed deposition and scour at the wide section, the forced bar in the channels with variable width are grouped into central and side bars [Bittner, 1994; Repetto et al., 2002; Wu and Yeh, 2005]. Figure 1-5(a) and Figure 1-6(a) display the experimental bed configurations of central and side bars [Bittner, 1994; Wu and Yeh, 2005]. In the numerical models the correction for the effect of secondary helical flow is necessary to simulate the forced bars. Figure 1-5 and Figure 1-6 display the model without helical flow would not predict the bed forms precisely. Repetto (2002) concluded that the wave number of width variation determines the bar type.

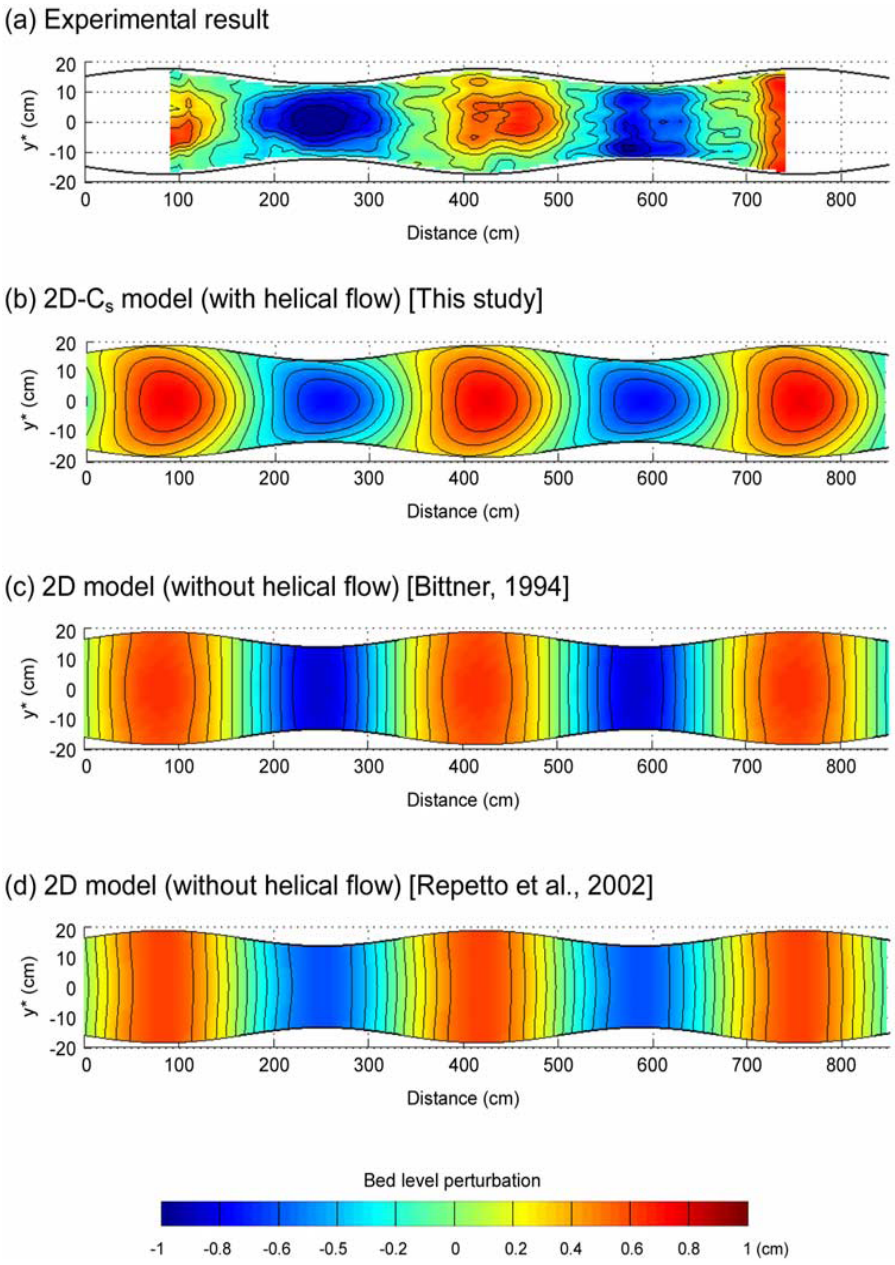

Figure 1-5 Contour plots showing (a) central bars observed in experiment [Wu and Yeh, 2005] and results of (b) 2-D-Cs model [Wu and Yeh, 2005], (c) 2-D model [Bittner, 1994], (d) 2-D model [Repetto et al., 2002]

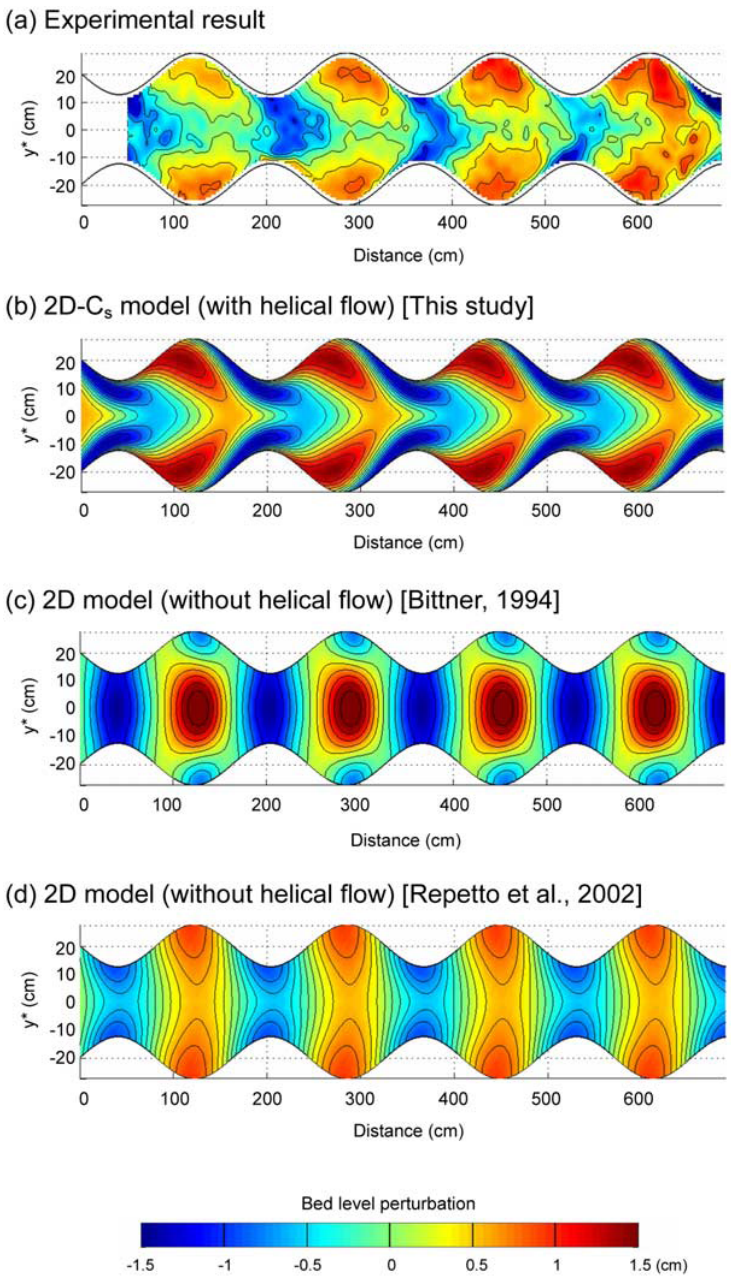

Figure 1-6 Contour plots showing (a) side bars observed in experiment [Bittner, 1994] and results of (b) 2-D-Cs model [Wu and Yeh, 2005], (c) 2-D model [Bittner, 1994], (d) 2-D model [Repetto et al., 2002]

Wu and Yeh (2005) further concluded that the variable-width induced forced bars are a function of width-to-depth ratio, dimensionless wave number of width variation, dimensionless shear stress of reference uniform flow and dimensionless grain size. The width-to-depth ratio and dimensionless wave number of width variation mainly determine the bed form development, however, dimensionless shear stress of reference uniform flow and grain size influence the bar height only. Figure 1-7 shows that the predictions of Wu and Yeh (2005) studies are in agreement with the experimental observations [Bittner, 1994; Wu and Yeh, 2005].

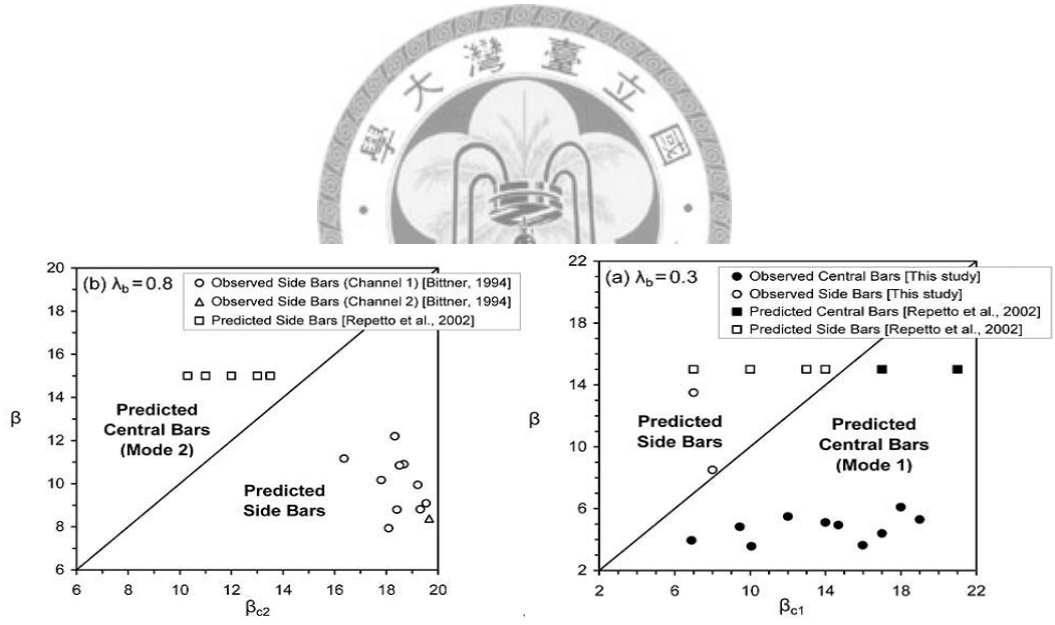

Figure 1-7 Comparisons between observed values of beta and corresponding values of BetaC1 and BetaC2. [Wu and Yeh, 2005]

1.2.3 Free bars affected by channel geometry

Kinoshita and Miwa (1974) first observed that the development of alternate bars is suppressed by channel curvature in their experiments. In particular, alternate bars do not develop when the channel sinuosity exceeds a threshold value. Turbino and Seminara (1990) used the perturbation expansion method to interpret this phenomenon theoretically with reference to a regular sequence of small-amplitude meanders. Their theory has the ability to determine the threshold value of channel curvature above which free bars are suppressed as a function of meander wavenumbe for given flow and sediment conditions. Whiting and Dietrich (1993) conducted a series of experiments to investigate the free bars migrating through channel bends and found that free bar migration was constrained by the wavelength of the meander channel. In their observations the migration of free bars were non-uniform and temporarily stalled when in phase with the curvature-induced topography. Figure 1-8 shows the experimental results regarding the unsteady migration of free bars through meanders.

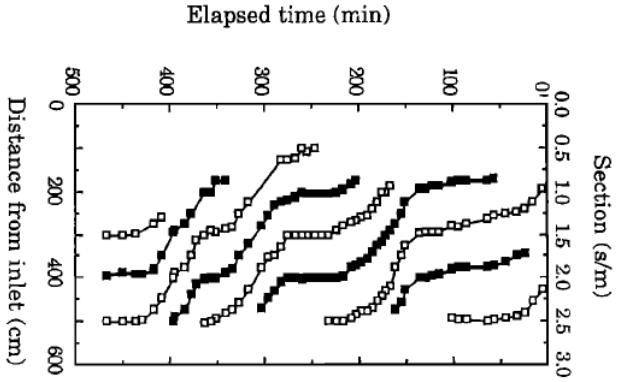

Figure 1-8 Unsteady migration of bars through meanders. Open squares indicate the position of leading edge of bars attached to the left bank; solid squares, the leading edge of bars attached to the right bank.

Lanzoni and Tubino (2001) conducted a series of flume experiments to study the free bars development in channels with variable width. They compared the bar height and bar wavelength of free bars in a straight channel and channels with variable width, and found that both of them are suppressed when encountering the width variation, as shown in Figure 1-9. Tubino et al. (2000) studied analytically the suppression of alternate bars exerted by the channel width variation. A perturbation method with linear stability theory was used to analyze this issue. As a result, the suppression of alternate bars in channels with width variation was characterized by a correction factor of growth rate of free bars. However, it is not able to discuss the bar height, wavelength and celerity influenced by width variation. Numerical experiments are expected to capture the coexistence of free and forced bars and performed in this study to investigate the influences of forcing effect on free bars.

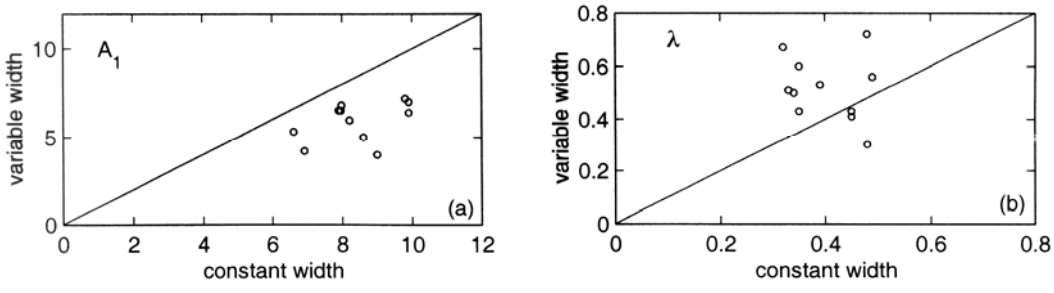

Figure 1-9 Comparison between measured values of (a) the amplitude and (b) dimensionless wavenumber of the leading Fourier component of bed topography associated with alternate bars in constant width and variable width experiments. [Lanzoni and Tubino, 2001]

1.2.4 Morphodynamic model

While 3D morphodynamic models can be used to study in detail the evolution of river morphology, 2D models are more efficient in practical applications. A number of researchers have devoted to the development of 2D morphodynamic models. Finite difference (FD) schemes have been commonly used to investigate the alluvial bend morphology and meandering channels. Koch and Folkstra (1981) applied a simplified 2D model to curved alluvial flumes of constant circular bends. Struiksma (1985) used a 2D FD model to reproduce the observed patterns of scour and deposition along a meandering reach of the Waal River. Struiksma et al. (1985) simulated the sour and deposition measured in the laboratory curved flumes. Shimizu and Itakura (1989) modeled the bed evolution in a sine-generated meandering channel. Kassem and Chaudhry (2002) applied a boundary fitted FD model to simulate some of the alluvial bend experiments of Koch and Folkstra (1981) and Struiksma et al. (1985).

The shortcoming of 2D morphodynamic models is that the momentum transport by secondary currents of 3D flow structures is neglected [Shimizu et al., 1990]. The streamline curvature is employed to reflect the effect of secondary flow for correcting the direction of sediment transport. The relation is expressed as follows [Engelund, 1974; Struiksma et al., 1985]:

$$\tan\delta_s = a\left(\frac{D_w}{r_c}\right) \qquad (1\text{-}1)$$

where δ_s is the angle between the bed shear stress and depth-average flow direction, D_w is flow depth, r_c is the local radius of curvature of the streamline, and a is a friction coefficient ranging between 5 and 12 [Engelund, 1974]. However, equation (1-1) tends to overestimate the effect of secondary flow in the case of strong curvature [Blanckaert and de Vriend, 2003; Blanckaert and Graf, 2004].

Vasquez (2005) incorporated the VAM model rather than the traditional VA

model into a 2D finite element (FE) morphodynamic model. VAM model assumes a vertical distribution of the velocity components across the flow depth, thus is by itself able to describe the secondary flows with the governing equations. Vasquez (2005) carried out numerical simulations on the scour and deposition in curved channels and meandering rivers by using VAM equations in the morphodynamic model. However, his model failed in the channels with variable width and the convection-dominated bed evolution because the streamline upwind Petrov-Galerkin (SUPG) scheme [Hicks and Steffler, 1992; Ghamry, 1999] was applied to the flow model but not to the bed evolution model [Vasquez, 2005]. The FE model with SUPG scheme has the ability to process the convective evolution of bed forms.

Nelson and Smith (1989) simulated the evolution of alternate bars using a standard FD scheme. The model reproduced the generation of free bars downstream an initial disturbance and the simulated results were similar to those observed by Fujita and Muramoto (1985). Defina (2003) used a 2D FE model to reproduce the experimental results of Lanzoni (2000), where migrating alternate bars developed in the straight channel from an initial flat bed. The initial disturbance was used in these numerical experiments to trigger the generation of free bars. Qualitatively speaking, the simulated results are in good agreement with the experimental results [Lanzoni, 2000] and the weakly nonlinear solutions [Colombini et al., 1987; Schielen et al., 1993]. However, different types of disturbance would lead to different bar characteristics. More recently, Bernini et al. (2006) simulated the generation of free bars in a straight, rectangular channel with both supercritical and subcritical uniform flows using the ADI scheme. The results were used to study the effect of gravity due to the transverse bed slope on the equilibrium geometric and kinematic bar characteristics. Although Defina (2003) and Bernini et al. (2006) successfully simulated the generation of free bars in straight, rectangular channels and

demonstrated qualitatively the agreement with experimental data and analytical solutions, none has incorporated the effect of secondary flow and simulated the case of variable-width channel.

1.3 Scope of Study

The aim of this study is to conduct numerical experiments to investigate the influences of the forcing effect on free bars. Wu used a morphodynamic model composed of the hydrodynamic and bed evolution equations, both of them belong to the hyperbolic equation. The streamline upwind Petrov Galerkin (SUPG) scheme is applied to both the hydrodynamic and bed evolution equations to overcome the defect for which the traditional Galerkin scheme may fail in the hyperbolic equation. The details of the numerical models are described in Chapter 2. The vertically averaged (VA) model is used in the hydrodynamic model. The applicability of the VA model in the morphodynamic model is validated and their accuracies are examined in Chapter 3. In the present study the VA model are chosen to conduct the numerical experiments due to its efficiency.

To investigate the influences of the forcing effect on free bars, a series of numerical experiments are conducted with different amplitudes and wave numbers of channel width variations. The ratios between the characteristics of the free bars developed in the variable-width and straight channels are used to describe the effect of channel width variations on free bars. These characteristics include the evolutions of bar height, wave length and celerity as the train of alternate bars passes through the periodic cycle of width variations. A forcing factor which quantifies the geometry of the channel with variable width is proposed to assess the influence of channel forcing effect on free bars. The numerical experiments and discussion are described in Chapter 4. Finally, overall conclusions are summarized in Chapter 5.

Chapter 2 Mathematical Model

In this chapter, the governing equations of hydrodynamics and bed evolution, along with their closure relations are described first. Then, the two-dimensional (2D) finite element (FE) morphodynamic model and the upwind scheme are presented.

2.1 Governing Equations of Hydrodynamic Model

The vertical average (VA) model is used in present study. It is derived from the fundamental full three-dimensional (3D) Reynolds equations. The full 3D Reynolds equations, including a continuity equation and three momentum equations, are given by

$$\frac{\partial U}{\partial x}+\frac{\partial V}{\partial y}+\frac{\partial W}{\partial z}=0 \tag{2-1a}$$

$$\frac{\partial U}{\partial t}+U\frac{\partial U}{\partial x}+V\frac{\partial U}{\partial y}+W\frac{\partial U}{\partial z}=-\frac{1}{\rho}\frac{\partial P}{\partial x}+\frac{1}{\rho}\left(\frac{\partial R_{xx}}{\partial x}+\frac{\partial R_{xy}}{\partial y}+\frac{\partial R_{xz}}{\partial z}\right) \tag{2-1b}$$

$$\frac{\partial V}{\partial t}+U\frac{\partial V}{\partial x}+V\frac{\partial V}{\partial y}+W\frac{\partial V}{\partial z}=-\frac{1}{\rho}\frac{\partial P}{\partial y}+\frac{1}{\rho}\left(\frac{\partial R_{yx}}{\partial x}+\frac{\partial R_{yy}}{\partial y}+\frac{\partial R_{yz}}{\partial z}\right) \tag{2-1c}$$

$$\frac{\partial W}{\partial t}+U\frac{\partial W}{\partial x}+V\frac{\partial W}{\partial y}+W\frac{\partial W}{\partial z}=-\frac{1}{\rho}\frac{\partial P}{\partial z}+\frac{1}{\rho}\left(\frac{\partial R_{wx}}{\partial x}+\frac{\partial R_{wy}}{\partial y}+\frac{\partial R_{wz}}{\partial z}\right) \tag{2-1d}$$

where (x,y,z) are the longitudinal-, transverse-, and vertical-direction coordinates, (U,V,W) are the velocities in the (x,y,z) directions, P is the pressure, ρ is the density of fluid, and R_{ij} is the Reynolds stress, defined as the stress in the j-direction acting on a face whose normal is in the i-direction. The VA model is derived from integrating equation (2-1) over the flow depth with a constant velocity, as described below. The shallow water approximation is adopted here, which implies that the

vertical accelerations is negligible compared to the gravity. It is further assumed that the pressure is hydrostatically distributed and flow separation is ignored. [Tubino and Repetto et al, 2000]

The velocity distributions across the whole flow depth are given by

$$\begin{cases} U_0 = \dfrac{\int_{z_b}^{z_b+D_w} U dz}{D_w} \\ V_0 = \dfrac{\int_{z_b}^{z_b+D_w} V dz}{D_w} \end{cases} \tag{2-2a}$$

where (U_0, V_0) are the depth average velocity components. To impose the kinematic bed and surface boundary condition to W leads to the following relation:

$$\int_{z_b}^{z_b+D_w} W dz = \frac{\partial D_w}{\partial t} + U_0 \frac{\partial D_w}{\partial x} + V_0 \frac{\partial D_w}{\partial y} \tag{2-2b}$$

Integrating (2-1) over the flow depth vertically from the bottom to the flow surface, with the relations (2-2a, b) and an assumption that P is the hydrostatic pressure, leads to the following three equations [Molls and Chaudhry, 1995; Ghamry, 1999]:

$$\frac{\partial D_w}{\partial t} + \frac{\partial Q_x}{\partial x} + \frac{\partial Q_y}{\partial y} = 0 \tag{2-3a}$$

$$\frac{\partial Q_x}{\partial t} + \frac{\partial}{\partial x}\left(\frac{Q_x^{\,2}}{D_w} + \frac{g D_w^{\,2}}{2} - \frac{D_w \overline{R}_{xx}}{\rho} \right) + \frac{\partial}{\partial y}\left(\frac{Q_x Q_y}{D_w} - \frac{D_w \overline{R}_{xy}}{\rho} \right) + g D_w \frac{\partial z_b}{\partial x} + \frac{\tau_x}{\rho} = 0 \tag{2-3b}$$

$$\frac{\partial Q_y}{\partial t} + \frac{\partial}{\partial x}\left(\frac{Q_x Q_y}{D_w} - \frac{D_w \overline{R}_{yx}}{\rho} \right) + \frac{\partial}{\partial y}\left(\frac{Q_y^{\,2}}{D_w} + \frac{g D_w^{\,2}}{2} - \frac{D_w \overline{R}_{yy}}{\rho} \right) + g D_w \frac{\partial z_b}{\partial y} + \frac{\tau_y}{\rho} = 0 \tag{2-3c}$$

where (Q_x, Q_y) and (τ_x, τ_y) are the unit discharges and bed shear stresses in the (x, y) directions. (D_w, Q_x, Q_y) need to be solved by equation (2-3).

2.2 Governing Equation of Bed Evolution Model

The governing equation of bed evolution is the sediment continuity equation, i.e., Exner equation. The processes involved in the Exner equation are bedform translation and diffusion [Lisle et al., 1997, 2001; Cui et al., 2003b], which describe different mechanisms of bed evolution. The Exner equation is given by

$$\left(1-\lambda_p\right)\frac{\partial z_b}{\partial t}+\frac{\partial Q_{bx}}{\partial x}+\frac{\partial Q_{by}}{\partial y}=0 \tag{2-4}$$

where $\left(Q_{bx},Q_{by}\right)$ are sediment transport rates in the $\left(x,y\right)$ directions; λ_p is the bed porosity.

2.2.1 Closure relations

Closure relations for $\overline{R}_{ij}$, $\left(\tau_x,\tau_y\right)$, and $\left(Q_{bx},Q_{by}\right)$ are needed. The vertically averaged Reynolds stresses $\overline{R}_{ij}$ are approximated with the Boussinesq model [Ghamry, 1999], i.e.,

$$\begin{cases}\overline{R}_{xx}=2\rho V_h\dfrac{\partial}{\partial x}\left(\dfrac{Q_x}{D_w}\right)\\ \overline{R}_{yy}=2\rho V_h\dfrac{\partial}{\partial y}\left(\dfrac{Q_y}{D_w}\right)\\ \overline{R}_{xy}=\overline{R}_{yx}=\rho V_h\left(\dfrac{\partial}{\partial x}\left(\dfrac{Q_y}{D_w}\right)+\dfrac{\partial}{\partial y}\left(\dfrac{Q_x}{D_w}\right)\right)\end{cases} \tag{2-5}$$

where V_h is the vertically averaged eddy viscosities in the horizontal directions. For simplicity, the case of bed-dominated turbulence is assumed, and the values of the order of $V_h=0.5U_*D_w$ is used here [Ghamry, 1999], where $U_*=\sqrt[4]{\left(\dfrac{\tau_x}{\rho}\right)^2+\left(\dfrac{\tau_y}{\rho}\right)^2}$ is the shear velocity, $\left(\tau_x,\tau_y\right)$ are expressed as

$$\begin{cases} \tau_x = \rho C_f U_0 \sqrt{U_0^{\,2} + V_0^{\,2}} \\ \tau_y = \rho C_f V_0 \sqrt{U_0^{\,2} + V_0^{\,2}} \end{cases} \tag{2-6}$$

where C_f is the bed friction coefficient, defined by

$$C_f = \left(2.5 \log \left(\frac{11 D_w}{K_s} \right) \right)^{-2} \tag{2-7}$$

where K_s is the roughness height, defined as 2.5 times the grain size [Cui et al., 1996, 2003a]. The sediment transport rates in the horizontal plane are defined as

$$\left(Q_{bx}, Q_{by} \right) = \left(\cos\alpha, \sin\alpha \right) Q_b \tag{2-8}$$

where α = angle between the sediment trajectory and x-direction, and is given by

$$\sin\alpha = \sin\chi - \frac{r}{\sqrt{\theta}} \frac{\partial z_b}{\partial y} \tag{2-9}$$

where r is an empirical coefficient reflecting the influence of transverse bed slope, and ranges between 0.3 and 1 [Talmon and Struiksma et al, 1995; Wu and Yeh, 2005]; θ= Shields stress; χ= angle between the local bed shear stress and x-direction, expressed as

$$\sin\chi = \frac{V_0}{\sqrt{U_0 + V_0}} - a D_w C_s \tag{2-10}$$

where a is the helical flow coefficient; C_s is the dimensionless local curvature of streamline [Wu and Yeh, 2005], defined by

$$C_s = \frac{-\frac{\partial}{\partial x}\left(\frac{V_0}{U_0} \right)}{\left(1 + \left(V_0 / U_0 \right)^2 \right)^{3/2}} \tag{2-11}$$

The angle χ accounts for the deviation of the zero-average helical flow from the

depth-averaged flow, driven by the bedform or channel variation.

The Meyer-Peter and Muller formula is suitable for evaluating the sediment transport rate of well-sorted grains [Wu and Yeh, 2005], which is given by

$$\Phi = 8\left(\theta - \theta_c\right)^{3/2} \tag{2-12}$$

where Φ is the bed load intensity, and $\theta_c \approx 0.04$ is the dimensionless critical shear stress. The sediment transport discharge Q_b could be evaluated by

$$Q_b = \Phi\sqrt{\frac{\left(\rho_s - \rho\right)}{\rho} g D_{sm}{}^3} \tag{2-13}$$

where ρ_s and D_{sm} are the density and average grain size of sediment, respectively.

2.3 Finite Element Method

2.3.1 Streamline upwind Petrov-Galerkin scheme

The term ‘upwind’ originates from the manner in which the discretization is applied depending on the direction of wave propagation. This wave can be the characteristic waves of the conservation laws or disturbance wave [Giraldo, 1995]. Godunov (1959) introduced the idea that the information from the exact local solution to the Euler equations could be included in the discretization for the purposes of computational studies. He applied this method to the finite volume (FV) method. Brooks and Hughes (1982) first applied this concept to the finite element (FE) method to solve the convection-dominated flow.

Dendy (1974) and Wahlbin (1974) derived the dissipative Gelerkin scheme to solve the first-order hyperbolic equations. Katopodes (1984) applied the dissipative Galerkin scheme to the non-conservation form of de St. Venant equations and simulated the 1D and 2D hydraulic jumps. The dissipative Galerkin scheme, however,

only considered the progressive characteristic velocity of the hydrodynamic equations in the upwinding term. The characteristic velocities of the hydrodynamic equations, in fact, include the progressive and reprogressive directions. Hughes and Mallet (1986) examined the application of the Petrov-Galerkin method to the symmetric systems of hyperbolic equations. Based on their work, Hicks and Steffler (1992) developed the characteristic dissipative Galerkin (CDG) scheme which used each of the characteristic velocities in determination of the upwinding matrix. Both of the above studies examined their models using the 1D hydrodynamic equations. Recently, Ghamry (1999) succeeded in applying the CDG scheme to solve the 2D vertically averaged and moment (VAM) equations.

The FE method employed in this study is the streamline upwind Petrov-Galerkin scheme [Brooks and Hughes, 1982]. The phrase 'streamline upwind' implies that the direction of advection is incorporated into the discretization, thus it is more suitable for hyperbolic equations than the traditional Bubnov-Galerkin scheme [Brooks and Hughes, 1982; Giraldo, 1995]. The advantage of using the FE method is that boundary conditions can be easily imposed on the discretized domain of natural environments with complicated geometry. Throughout this study, triangular elements are used for discretization of the computational domain.

The governing equations of the VA model has a general form that can be expressed as

$$\frac{\partial \varphi}{\partial t}+\frac{\partial \mathbf{f}_x(\varphi)}{\partial x}+\frac{\partial \mathbf{f}_y(\varphi)}{\partial y}+\mathbf{S}_t(\varphi)=0 \qquad (2\text{-}14)$$

where φ is the solution of the governing equations; $\mathbf{f}_x(\varphi)$ and $\mathbf{f}_y(\varphi)$ are the flux vectors in the x- and y-direction; $\mathbf{S}_t(\varphi)$ is the source vector. For the VA model, $\varphi=\{D_w;Q_x;Q_y\}$. The discretization of the computation domain are treated with

triangular elements, then the approximate solution of an element is given by

$$\tilde{\varphi}^e = \sum_{i=1}^{3} N_i^e \zeta_i^e \tag{2-15}$$

where N_i^e is the shape function of node *i*, the Lagrange interpolation function is used in this study; ζ_i is the solution of node *i*. Substituting (2-15) into (2-14), multiplying the resulting equation with a specified weighting function and integrating it over an element domain Ω_e leads to the general form of the equation for streamline upwind Petrov-Galerkin scheme [Hicks and Steffler, 1992]:

$$\int_{\Omega_e} \hat{\mathbf{N}}_i^e \left(\frac{\partial \tilde{\varphi}^e}{\partial t} + \frac{\partial \mathbf{f}_x\left(\tilde{\varphi}^e\right)}{\partial x} + \frac{\partial \mathbf{f}_y\left(\tilde{\varphi}^e\right)}{\partial y} + \mathbf{S}_t\left(\tilde{\varphi}^e\right) \right) d\Omega_e = 0 \quad \text{for} \quad i = 1,2,3 \tag{2-16a}$$

where $\hat{\mathbf{N}}_i^e$ is the weighting function matrix of node *i* in an element, which is defined as :

$$\hat{\mathbf{N}}_i^e = \mathbf{N}_i^e + \mathbf{W}_i^e = \begin{bmatrix} N_i^e & 0 & 0 \\ 0 & N_i^e & 0 \\ 0 & 0 & N_i^e \end{bmatrix} + \left(\omega \Delta x \mathbf{W}_x^e \frac{\partial \mathbf{N}_i^e}{\partial x} + \omega \Delta y \mathbf{W}_y^e \frac{\partial \mathbf{N}_i^e}{\partial y} \right) \tag{2-16b}$$

where $\mathbf{N}_i^e$ is a diagonal matrix of N_i^e; ω is an upwind coefficient ranging from 0.25 to 0.75, in this study a value of 0.5 is used (Note that (2-16) would reduce to the traditional Bubnov-Galerkin scheme if $\omega = 0$); the element sizes $\triangle x = \triangle y = \frac{\sqrt{A_e}}{2}$, with A_e = element area [Ghamry, 1999]; $\mathbf{W}_x^e$ and $\mathbf{W}_y^e$ are the upwind matrices in the x- and y-direction, which characterize the advection mechanism and are the key terms in (2-16). To specify $\mathbf{W}_x^e$ and $\mathbf{W}_y^e$, a characteristic dissipative Galerkin (CDG) scheme is adopted here [Hicks and Steffler, 1992; Ghamry, 1999], which gives

$$\begin{cases} \mathbf{W}_x^{\,e} = \mathbf{A}_x \left(\sqrt{\mathbf{A}_x^{\,2} + \mathbf{A}_y^{\,2}} \right)^{-1} \\ \mathbf{W}_y^{\,e} = \mathbf{A}_y \left(\sqrt{\mathbf{A}_x^{\,2} + \mathbf{A}_y^{\,2}} \right)^{-1} \end{cases} \tag{2-17}$$

where $\mathbf{A}_x$ and $\mathbf{A}_y$ are the advection matrices in the x- and y-direction, respectively, which are derived from (2-14) and expressed as follows:

$$\frac{\partial \varphi}{\partial t} + \mathbf{A}_x \frac{\partial \varphi}{\partial x} + \mathbf{A}_y \frac{\partial \varphi}{\partial y} + \mathbf{S}_t(\varphi) = 0 \tag{2-18}$$

The details regarding the applications of the CDG scheme to the flow dynamics and bed evolution models are described below. The general forms of $\mathbf{A}_x$ and $\mathbf{A}_y$ are defined as

$$\mathbf{A}_x = \begin{bmatrix} \frac{\partial f_x(\varphi)_{\mathrm{c}}}{\partial D_w} & \frac{\partial f_x(\varphi)_{\mathrm{c}}}{\partial Q_x} & \frac{\partial f_x(\varphi)_{\mathrm{c}}}{\partial Q_y} \\ \frac{\partial f_x(\varphi)_{\mathrm{mx}}}{\partial D_w} & \frac{\partial f_x(\varphi)_{\mathrm{mx}}}{\partial Q_x} & \frac{\partial f_x(\varphi)_{\mathrm{mx}}}{\partial Q_y} \\ \frac{\partial f_x(\varphi)_{\mathrm{my}}}{\partial D_w} & \frac{\partial f_x(\varphi)_{\mathrm{my}}}{\partial Q_x} & \frac{\partial f_x(\varphi)_{\mathrm{my}}}{\partial Q_y} \end{bmatrix} \tag{2-19a}$$

$$\mathbf{A}_y = \begin{bmatrix} \frac{\partial f_y(\varphi)_{\mathrm{c}}}{\partial D_w} & \frac{\partial f_y(\varphi)_{\mathrm{c}}}{\partial Q_x} & \frac{\partial f_y(\varphi)_{\mathrm{c}}}{\partial Q_y} \\ \frac{\partial f_y(\varphi)_{\mathrm{mx}}}{\partial D_w} & \frac{\partial f_y(\varphi)_{\mathrm{mx}}}{\partial Q_x} & \frac{\partial f_y(\varphi)_{\mathrm{mx}}}{\partial Q_y} \\ \frac{\partial f_y(\varphi)_{\mathrm{my}}}{\partial D_w} & \frac{\partial f_y(\varphi)_{\mathrm{my}}}{\partial Q_x} & \frac{\partial f_y(\varphi)_{\mathrm{my}}}{\partial Q_y} \end{bmatrix} \tag{2-19b}$$

where the subscripts c, mx, my refer to the continuity equation, momentum equations in the x- and y-direction, respectively. The specific forms of $\mathbf{A}_x$ and $\mathbf{A}_y$ can be derived from (2-3), and are given by

$$\mathbf{A}_x = \begin{bmatrix} 0 & 1 & 0 \\ gD_w - U_0^2 & 2U_0 & 0 \\ -U_0V_0 & V_0 & U_0 \end{bmatrix} \tag{2-20a}$$

$$\mathbf{A}_y = \begin{bmatrix} 0 & 0 & 1 \\ -U_0V_0 & V_0 & U_0 \\ gD_w - V_0^2 & 0 & 2V_0 \end{bmatrix} \tag{2-20b}$$

The eigenvalues of (2-20) are the characteristic celerity of the system of equations (2-3) [Hicks and Steffler, 1992], the reason why it is called 'characteristic dissipative Gelerkin' scheme. The eigenvalues of the advection matrices of the VA model, U_0, $U_0 + \sqrt{gD_w}$, and $U_0 - \sqrt{gD_w}$, are the characteristic celerity of (2-3). To calculate the inverse of $\sqrt{\mathbf{A}_x^2 + \mathbf{A}_y^2}$ in (2-17), the numerical procedure based on the Cayley-Hamilton theorem is employed [Hoger and Carlson, 1984].

2.3.2 Applying CDG scheme to bed evolution model

While the CDG scheme has been successfully applied to flow dynamics models, to date applying the CDG scheme to solve the sediment continuity equation has never been carried out due to the complexities involved in the formulation [Vasquez, 2005]. In the river morphology model of Vasques (2005) only the hydrodynamic model applied the CDG scheme and the bed evolution model was treated with a hybrid method. As a results, the point bars in the bend were successfully simulated but the free bars and the force bars in the channels with variable width were not reproduced. It is demonstrated that applying the CDG scheme to the bed evolution may overcome such defects. Because the morphodynamic model is unable to capture the advection mechanism of bed evolution without incorporating an upwind scheme, some simplifications must be made in the formulation. As such, equations (2-3) and (2-4) are modified as

$$\frac{\partial U_0}{\partial x}+\frac{\partial V_0}{\partial y}=0 \tag{2-21a}$$

$$\frac{\partial U_0}{\partial t}+U_0\frac{\partial U_0}{\partial x}+V_0\frac{\partial U_0}{\partial y}+g\frac{\partial\left(D_w+z_b\right)}{\partial x}+\frac{\tau_x}{\rho D_w}=0 \tag{2-21b}$$

$$\frac{\partial V_0}{\partial t}+U_0\frac{\partial V_0}{\partial x}+V_0\frac{\partial V_0}{\partial y}+g\frac{\partial\left(D_w+z_b\right)}{\partial y}+\frac{\tau_y}{\rho D_w}=0 \tag{2-21c}$$

$$\left(1-\lambda_p\right)\frac{\partial z_b}{\partial t}+\cos\alpha\frac{\partial Q_b}{\partial x}+\sin\alpha\frac{\partial Q_b}{\partial y}=0 \tag{2-21d}$$

Since Q_b is a function of bed shear stress τ, the gradients of Q_b in the x- and y-direction may be rewritten as

$$\frac{\partial Q_b}{\partial x}=\frac{\partial Q_b}{\partial \tau}\frac{\partial \tau}{\partial x}=\frac{\partial Q_b}{\partial \tau}2\rho C_f\left(U_0\frac{\partial U_0}{\partial x}+V_0\frac{\partial V_0}{\partial x}\right) \tag{2-22a}$$

$$\frac{\partial Q_b}{\partial y}=\frac{\partial Q_b}{\partial \tau}\frac{\partial \tau}{\partial y}=\frac{\partial Q_b}{\partial \tau}2\rho C_f\left(U_0\frac{\partial U_0}{\partial y}+V_0\frac{\partial V_0}{\partial y}\right) \tag{2-22b}$$

Multiplying equations (2-21b) and (2-21c) by U_0 and V_0, respectively, and then summing up the resulting equations leads to

$$U_0\left(U_0\frac{\partial U_0}{\partial x}+V_0\frac{\partial V_0}{\partial x}\right)+V_0\left(U_0\frac{\partial U_0}{\partial y}+V_0\frac{\partial V_0}{\partial y}\right)+gU_0\frac{\partial z_b}{\partial x}+gV_0\frac{\partial z_b}{\partial y}+S_t{}'=0 \tag{2-23}$$

Substituting equation (2-23) into equation (2-22) gives

$$\frac{\partial Q_b}{\partial x}=\frac{\partial Q_b}{\partial \tau}2\rho g C_f\left(\frac{U_0}{U_0}\frac{\partial z_b}{\partial x}+\frac{V_0}{U_0}\frac{\partial z_b}{\partial y}+S_{t1}\right) \tag{2-24a}$$

$$\frac{\partial Q_b}{\partial y}=\frac{\partial Q_b}{\partial \tau}2\rho g C_f\left(\frac{U_0}{V_0}\frac{\partial z_b}{\partial x}+\frac{V_0}{V_0}\frac{\partial z_b}{\partial y}+S_{t2}\right) \tag{2-24b}$$

where S_{t1} and S_{t2} are the source terms, whose values do not affect the final results. Substituting equation (2-24) into equation (2-21d) gives

$$\left(\cos\alpha\frac{\partial Q_b}{\partial x},\ \sin\alpha\frac{\partial Q_b}{\partial y}\right)=2\rho g C_f\left(\frac{\cos\alpha}{U_0}+\frac{\sin\alpha}{V_0}\right)\left(U_0\frac{\partial z_b}{\partial x},\ V_0\frac{\partial z_b}{\partial y}\right) \tag{2-25}$$

Equation (2-25) implies that flow dynamics is the main driving force for the advection of bed deformations, while the contributions of bed slope and gravity are categorized

as the diffusion mechanism. Substituting equations (2-24) and (2-25) into (2-21d) would result in

$$\left(1-\lambda_p\right)\frac{\partial z_b}{\partial t}+C'\left(U_0\frac{\partial z_b}{\partial x}+V_0\frac{\partial z_b}{\partial y}\right)+S_{t3}=0 \tag{2-26}$$

where C' is a constant; S_{t3} is the source term. Equation (2-25) is similar to (2-18), however, the upwind matrices become two upwind components, which are given by

$$\left(W_{z_b,x},\ W_{z_b,y}\right)=\left(\frac{U_0}{\sqrt{U_0{}^2+V_0{}^2}},\frac{V_0}{\sqrt{U_0{}^2+V_0{}^2}}\right)=\left(\cos\chi,\sin\chi\right) \tag{2-27}$$

2.4 Model implementation

To implement the morphodynamic model, the flow is assumed to be quasi-steady. The time derivative terms in the governing equations of the VA model can be neglected, implying that the flow adapts to the altering bed topography immediately. Such a morphodynamic model is essentially a decoupled one. The flow, sediment, and bed topography computations are executed iteratively with the following procedure:

Step 1: Solve the flow dynamics model with the given bed topography.

Step 2: Evaluate the sediment transport rates with the calculated bed shear stress.

Step 3: Compute the bed topography at the next time using the bed evolution model.

Step 4: Go back to step 1 with the updated bed topography.

Implementations of the flow dynamics and bed evolution models are described below.

Implementing the flow dynamics model with the CDG scheme is described here. The weak form of the finite element equation and boundary conditions are introduced first. The Newton-Raphson algorithm is then adopted to solve the resulting system of equations.

Equation (2-3) may be rewritten in the form of (2-16a) as the following:

$$\int_{\Omega_e} \hat{\mathbf{N}}^e_{\mathrm{m},i} \left(\frac{\partial}{\partial x} \begin{bmatrix} f_x\left(\tilde{\varphi}^e\right)_{\mathrm{c}} \\ f_x\left(\tilde{\varphi}^e\right)_{\mathrm{mx}} \\ f_x\left(\tilde{\varphi}^e\right)_{\mathrm{my}} \end{bmatrix} + \frac{\partial}{\partial y} \begin{bmatrix} f_y\left(\tilde{\varphi}^e\right)_{\mathrm{c}} \\ f_y\left(\tilde{\varphi}^e\right)_{\mathrm{mx}} \\ f_y\left(\tilde{\varphi}^e\right)_{\mathrm{my}} \end{bmatrix} + \begin{bmatrix} S_t\left(\tilde{\varphi}^e\right)_{\mathrm{c}} \\ S_t\left(\tilde{\varphi}^e\right)_{\mathrm{mx}} \\ S_t\left(\tilde{\varphi}^e\right)_{\mathrm{my}} \end{bmatrix} \right) d\Omega_e = 0\,, \quad i = 1,2,3 \qquad (2\text{-}28)$$

Given (2-16b) and (2-17), the expansion of the weighting function matrix $\hat{\mathbf{N}}^e_{\mathrm{m},i}$ is

$$\hat{\mathbf{N}}^e_{\mathrm{m},i} = \begin{bmatrix} N_i^e & 0 & 0 \\ 0 & N_i^e & 0 \\ 0 & 0 & N_i^e \end{bmatrix} + \begin{bmatrix} W_{\text{c-c}} & W_{\text{c-mx}} & W_{\text{c-my}} \\ W_{\text{mx-c}} & W_{\text{mx-mx}} & W_{\text{mx-my}} \\ W_{\text{my-c}} & W_{\text{my-mx}} & W_{\text{my-my}} \end{bmatrix} \qquad (2\text{-}29a)$$

where each element of the upwind matrix, denoted as $W_{\text{eq1-eq2}}$, represents the weighted contribution of equation 2 on upwinding of equation 1. For example, $W_{\text{c-mx}}$ represents the weighted contribution of the momentum equation in the x-direction on upwinding of the continuity equation.

Equations (2-28) and (2-29) may be combined and expressed as the following system of equations:

$$\int_{\Omega_e} \left(\mathbf{N}_i^e + \mathbf{W}_i^e \right) \left(\frac{\partial}{\partial x}\left[\mathbf{f}_x\left(\tilde{\varphi}^e\right)\right] + \frac{\partial}{\partial y}\left[\mathbf{f}_y\left(\tilde{\varphi}^e\right)\right] + \left[\mathbf{S}_t\left(\tilde{\varphi}^e\right)\right] \right) d\Omega_e = 0 \qquad (2\text{-}30)$$

where

$$\mathbf{W}_i^e = \omega \left(\triangle x \frac{\mathbf{A}_x}{\sqrt{\mathbf{A}_x^{\,2} + \mathbf{A}_y^{\,2}}} \frac{\partial \mathbf{N}_i^e}{\partial x} + \triangle y \frac{\mathbf{A}_y}{\sqrt{\mathbf{A}_x^{\,2} + \mathbf{A}_y^{\,2}}} \frac{\partial \mathbf{N}_i^e}{\partial y} \right) \qquad (2\text{-}30a)$$

$$\mathbf{f}_x\left(\tilde{\varphi}^e\right) = \begin{bmatrix} f_x\left(\tilde{\varphi}^e\right)_{\mathrm{c}} \\ f_x\left(\tilde{\varphi}^e\right)_{\mathrm{mx}} \\ f_x\left(\tilde{\varphi}^e\right)_{\mathrm{my}} \end{bmatrix} = \begin{bmatrix} \tilde{Q}_x^{\,e} \\ \dfrac{\tilde{Q}_x^{\,e2}}{\tilde{D}_w^{\,e}} + \dfrac{g\tilde{D}_w^{\,e2}}{2} - \dfrac{\tilde{D}_w^{\,e}\overline{\tilde{R}}_{xx}^{\,e}}{\rho} \\ \dfrac{\tilde{Q}_x^{\,e}\tilde{Q}_y^{\,e}}{\tilde{D}_w^{\,e}} - \dfrac{\tilde{D}_w^{\,e}\overline{\tilde{R}}_{yx}^{\,e}}{\rho} \end{bmatrix} \qquad (2\text{-}30b)$$

$$\mathbf{f}_y\left(\tilde{\varphi}^e\right) = \begin{bmatrix} f_y\left(\tilde{\varphi}^e\right)_{\mathrm{c}} \\ f_y\left(\tilde{\varphi}^e\right)_{\mathrm{mx}} \\ f_y\left(\tilde{\varphi}^e\right)_{\mathrm{my}} \end{bmatrix} = \begin{bmatrix} \tilde{Q}_y^{\,e} \\ \dfrac{\tilde{Q}_x^{\,e}\tilde{Q}_y^{\,e}}{\tilde{D}_w^{\,e}} - \dfrac{\tilde{D}_w^{\,e}\overline{\tilde{R}}_{xy}^{\,e}}{\rho} \\ \dfrac{\tilde{Q}_y^{\,e2}}{\tilde{D}_w^{\,e}} + \dfrac{g\tilde{D}_w^{\,e2}}{2} - \dfrac{\tilde{D}_w^{\,e}\overline{\tilde{R}}_{yy}^{\,e}}{\rho} \end{bmatrix} \qquad (2\text{-}30c)$$

$$\mathbf{S}_t\left(\tilde{\varphi}^e\right)=\begin{bmatrix} S_t\left(\tilde{\varphi}^e\right)_{\mathrm{c}} \\ S_t\left(\tilde{\varphi}^e\right)_{\mathrm{mx}} \\ S_t\left(\tilde{\varphi}^e\right)_{\mathrm{my}} \end{bmatrix}=\begin{bmatrix} 0 \\ g\tilde{D}_w{}^e\dfrac{\partial \tilde{z}_b{}^e}{\partial x}+\dfrac{\tilde{\tau}_x{}^e}{\rho} \\ g\tilde{D}_w{}^e\dfrac{\partial \tilde{z}_b{}^e}{\partial y}+\dfrac{\tilde{\tau}_y{}^e}{\rho} \end{bmatrix} \tag{2-30d}$$

To impose the boundary conditions, the weak form of (2-30) is used, as expressed by

$$\begin{aligned} &\int_{\Omega_e}\left\{\begin{aligned}&\mathbf{N}_i{}^e\left[\mathbf{S}_t\left(\tilde{\varphi}^e\right)\right]-\left[\mathbf{f}_x\left(\tilde{\varphi}^e\right)\right]\frac{\partial \mathbf{N}_i{}^e}{\partial x}-\left[\mathbf{f}_y\left(\tilde{\varphi}^e\right)\right]\frac{\partial \mathbf{N}_i{}^e}{\partial y}\\ &+\mathbf{W}_i^e\left(\frac{\partial}{\partial x}\left[\mathbf{f}_x\left(\tilde{\varphi}^e\right)\right]+\frac{\partial}{\partial y}\left[\mathbf{f}_y\left(\tilde{\varphi}^e\right)\right]+\left[\mathbf{S}_t\left(\tilde{\varphi}^e\right)\right]\right)\end{aligned}\right\}d\Omega_e \\ &+\int_{\Gamma_e}\mathbf{N}_i{}^e\left(\mathbf{f}_x\left(\tilde{\varphi}^e\right)n_x+\mathbf{f}_y\left(\tilde{\varphi}^e\right)n_y\right)d\Gamma_e=0\end{aligned} \tag{2-31}$$

where Γ_e is the segment of the boundary element; n_x and n_y denote the x- and y-component of the outward vector normal to Γ_e. The fluid flux across the boundary segment is expressed as $Q_n=f_x\left(\tilde{\varphi}^e\right)_{\mathrm{c}}n_x+f_y\left(\tilde{\varphi}^e\right)_{\mathrm{c}}n_y$ which is given by

$$q_0=Q_xn_x+Q_yn_y \tag{2-32}$$

where q_0 is the unit discharge. q_0 is a specified unit discharge at the upstream. The values of q_0 equal to zero at the wall boundary but treated as unknowns at the downstream boundary [Ghamry, 1999; Vasquez, 2005].

The Newton-Raphson algorithm is used to solve the system of equations (2-31). The general form of this algorithm is given by

$$\mathbf{J}^m\delta\tilde{\varphi}=-\mathbf{R}^m \tag{2-33}$$

where the superscript m is the iteration index; $\mathbf{R}^m$ is the global residual vector in m th iteration, for example,

$$\left[\mathbf{R}_i^e\right]^m = \int_{\Omega_e} \left\{ \begin{array}{l} \mathbf{N}_i^e \left[\mathbf{S}_t\left(\tilde{\varphi}^e\right)\right] - \left[\mathbf{f}_x\left(\tilde{\varphi}^e\right)\right]\dfrac{\partial \mathbf{N}_i^e}{\partial x} - \left[\mathbf{f}_y\left(\tilde{\varphi}^e\right)\right]\dfrac{\partial \mathbf{N}_i^e}{\partial y} \\ + \mathbf{W}_i^e\left(\dfrac{\partial}{\partial x}\left[\mathbf{f}_x\left(\tilde{\varphi}^e\right)\right] + \dfrac{\partial}{\partial y}\left[\mathbf{f}_y\left(\tilde{\varphi}^e\right)\right] + \left[\mathbf{S}_t\left(\tilde{\varphi}^e\right)\right]\right) \end{array} \right\}^m d\Omega_e$$
$$+ \int_{\Gamma_e} \mathbf{N}_i^e \left(\mathbf{f}_x\left(\tilde{\varphi}^e\right) n_x + \mathbf{f}_y\left(\tilde{\varphi}^e\right) n_y\right)^m d\Gamma_e \qquad (2\text{-}34)$$

where $\mathbf{R}_i^e$ is the residual vector of element *e* respect to the node *i* in (2-31). As a result, $\mathbf{R}$ is the assembly of $\mathbf{R}_i^e$. $\mathbf{J}$ is the global Jacobian matrix of (2-34), and is the result from the combination of local element Jacobian matrix which is defined as follows :

$$\left[\mathbf{J}_i^e\right]^m = \left[\frac{\partial \mathbf{R}^e}{\partial \tilde{D}_w{}^e}, \frac{\partial \mathbf{R}^e}{\partial \tilde{Q}_x{}^e}, \frac{\partial \mathbf{R}^e}{\partial \tilde{Q}_y{}^e}\right]^m \qquad (2\text{-}35)$$

; $\delta\tilde{\varphi}$ is the difference between the solutions from consecutive iterations. After each iteration the solution $\tilde{\varphi}$ is modified until $\delta\tilde{\varphi} \to 0$:

$$\tilde{\varphi}^{m+1} = \tilde{\varphi}^m + \delta\tilde{\varphi}^m = \left[\tilde{D}_w; \tilde{Q}_x; \tilde{Q}_y\right]^{m+1} \qquad (2\text{-}36)$$

Finally, when the error norm $\varepsilon^{m+1} = \left(\sqrt{\dfrac{\sum\left(\delta\tilde{\varphi}^m\right)}{\sum\tilde{\varphi}^2}}\right)^{m+1}$ is $\leq$ a user specified tolerance (typically 10^{-6}), the solution are convergent and $\tilde{\varphi}^{m+1}$ are the solution of fluid dynamic model.

Once the flow equations are solved, the bed shear stress and sediment transport rate can be evaluated. The bed evolution equation in the weak form is given by

$$\left[\int_{\Omega_e}\left(\mathbf{N}_i^e + \mathbf{W}_{z_b,i}{}^e\right) d\Omega_e\right] z_b{}^{t+1} = \left[\int_{\Omega_e}\left(\mathbf{N}_i^e + \mathbf{W}_{z_b,i}{}^e\right) d\Omega_e\right] z_b{}^t$$
$$- \frac{\Delta t}{1-\lambda_p}\left(\int_{\Omega_e} Q_{bx}{}^e \frac{\partial \mathbf{N}_i^e}{\partial x} + Q_{by}{}^e \frac{\partial \mathbf{N}_i^e}{\partial y} - \mathbf{W}_{z_b,i}{}^e\left(\frac{\partial Q_{bx}{}^e}{\partial x} + \frac{\partial Q_{by}{}^e}{\partial y}\right) d\Omega_e + \int_{\Gamma_e} \mathbf{N}_i{}^e Q_b{}^e d\Gamma_e\right)$$

(2-37)

where $\mathbf{W}_{z_b,i} = \omega\left(\triangle x W_{z_b,x}{}^{e} \frac{\partial \mathbf{N}_i^{e}}{\partial x} + \triangle y W_{z_b,y}{}^{e} \frac{\partial \mathbf{N}_i^{e}}{\partial y} \right)$. The bed elevation at the next time step z_b^{t+1} is directly obtained by solving (2-37).

Chapter 3 Model Validation

In this chapter, the simulation results of the flow dynamics and morphodynamic models are validated. The flow dynamics model is validated with the experimental data of a variable-width channel. The morphodynamics model is validated with the data of force bars (side bars and central bars), free migrating alternate bars and a simulation case of coexistence of free and forced bars.

3.1 Validation of Hydrodynamics Model

3.1.1 Channel with variable width

Bittner (1994) conducted a series of experiments in channels with variable width. One of these experiments, run C1-11, in which depths of flow were measured over the developed bedforms (side bars), was used here to validate the flow dynamics models. The sidewall of the channel was sinusoidal, with its width variation described by

$$B^* = B_0 + b_0 \sin\left(\frac{2\pi}{\lambda_c} x\right) \tag{3-1}$$

where $B^* =$ channel half-width at x, here $x =$ longitudinal coordinate; $B_0 =$ mean half-width = 0.2 m; $b_0 =$ width perturbation = 0.075 m; $\lambda_c =$ wavelength of channel width variation = 1.6 m.

The simultaneously measured final bed topography and flow depth in the four cycles of the channel width variations are shown in Figure 3-1, where both the bed deformation and flow depth exhibit repeated patterns. To compute the flow, the final bed deformations in these four cycles were averaged and used as the input fixed-bed topography to the flow dynamics models (Figure 3-2), leading to the repeated flow patterns in the four cycles.

The computation domain is shown in Figure 3-3a, where 1,326 nodes and 2,400 elements are contained in the six cycles. The zoomed-in element mesh in a cycle of width variation is demonstrated in Figure 3-3b. The boundary condition imposed at the upstream is the unit discharge $q_0 = 0.0073$ m^2/s. No boundary condition was specified at the downstream. No-penetration was used at the sidewall, where the streamline is parallel with the channel wall. The bed roughness height $K_s = 0.0013$ m was used.

The computed results of flow depth are shown in Figure 3-4, where the results of the VA models are similar to the measured results shown in Figure 3-1b, i.e., greater flow depths at the narrower sections and smaller depths at the wider sections, especially over the side bars. Detailed comparisons of the computed and measured results at the four specified sections of a cycle (indicated in Figure 3-3b) are shown in Figure 3-5, where good agreement between the computed and measured results are demonstrated. Only at the 3/4πsection, the VA models slightly under predicts the flow depth. The under predicted flow depth at the 3/4π section is attributed to the flow separation occurring at the 2/4π section, resulting in decreasing the pressure and raising the flow depth. Failing in the flow separation are attributed to the assumption that pressure has a hydrostatic distribution.

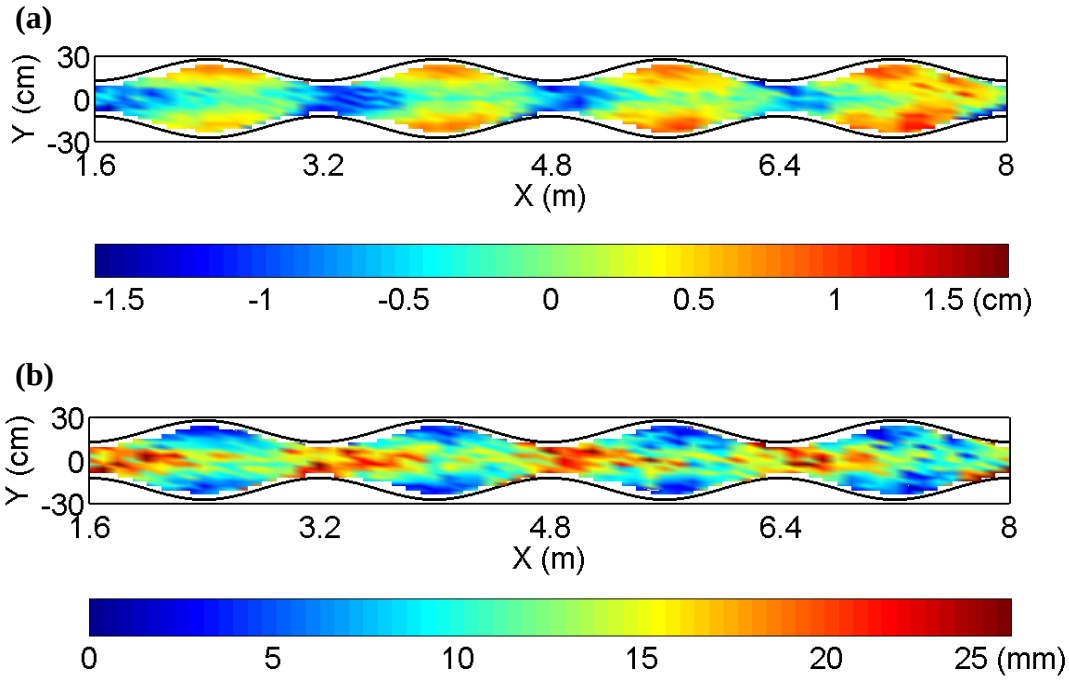

Figure 3-1 Measured results of (a) bed deformation, and (b) flow depth in Run C1-11 [Bittner, 1994]

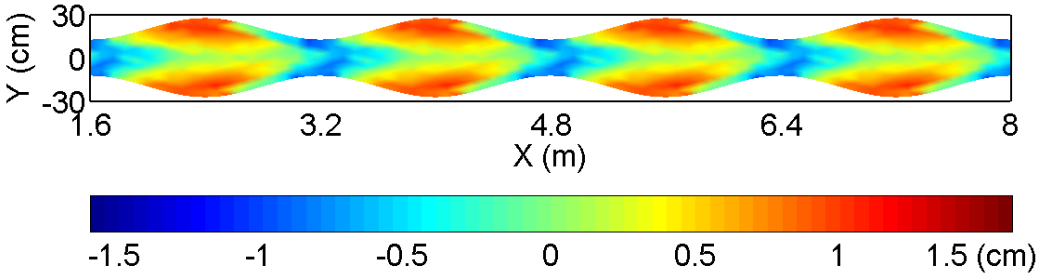

Figure 3-2 Averaged bed deformation of Run C1-11 [Bittner, 1994] used as the fixed-bed topography in the validation of the flow dynamics models

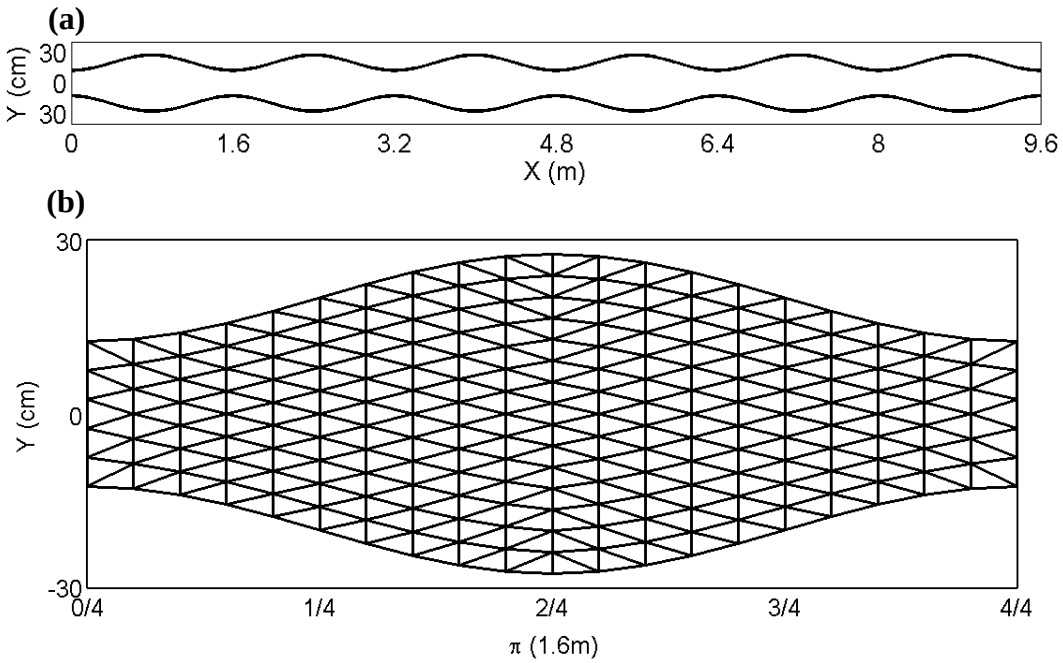

Figure 3-3 (a) Computation domain of Run C1-11 [Bittner, 1994] used in the validation of the hydrodynamics models; (b) zoomed-in element mesh in a cycle of width variation, the wavelength of a cycle (π) is 1.6m

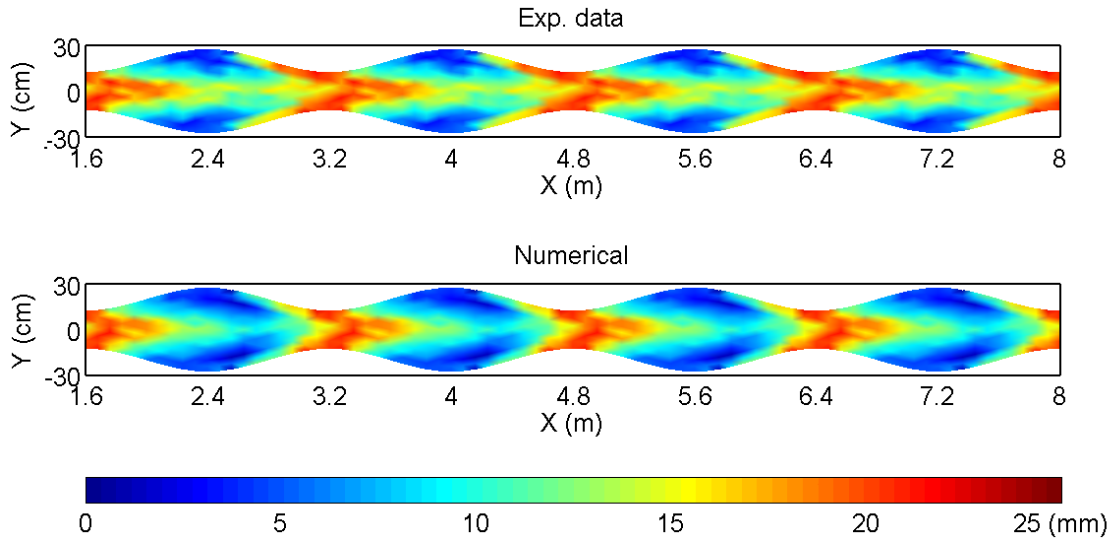

Figure 3-4 Computed Run C1-11 [Bittner, 1994] results of flow depth by the VA models

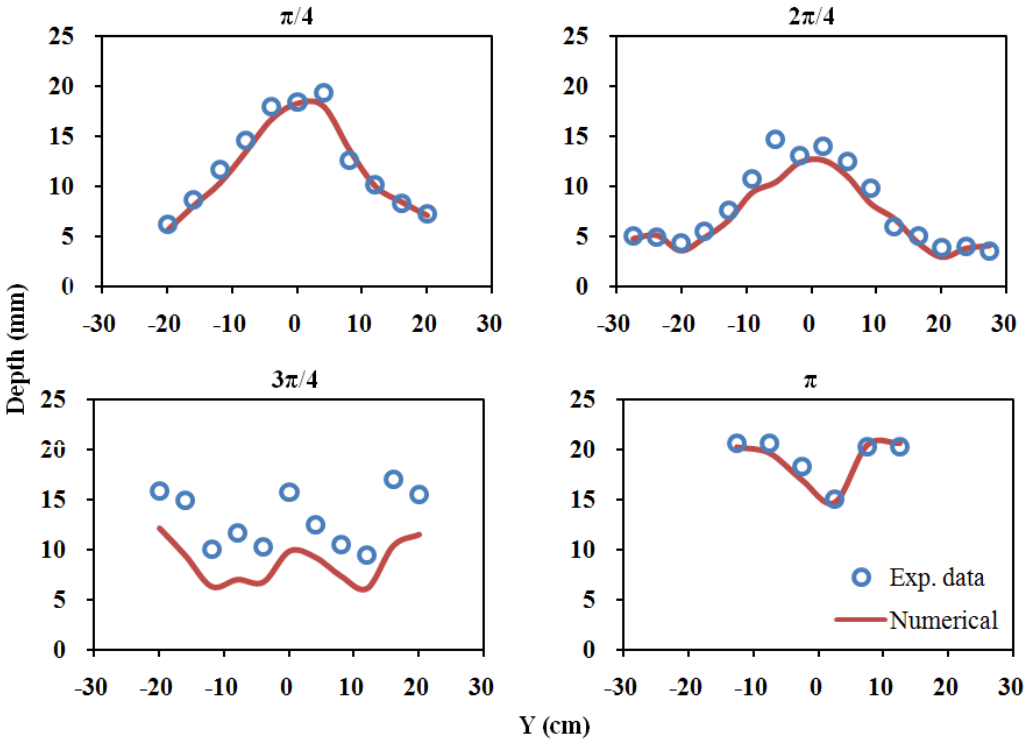

Figure 3-5 Comparison of measured and computed Run C1-11's [Bittner, 1994] results of flow depth at four specified sections of a cycle of width variation

3.2 Validation of Bed Evolution Model

The bed evolution model is validated with five types of bedforms, including two of forced bars (side bars and central bars), one of free migrating alternate bars and two of coexistence of free and forced bars. These results suggest that the CDG scheme may be applied to the sediment continuity equation without incorporating any artificial smoothing [Vasquez et al., 2007].

3.2.1 Forced bars – side bars

The bed topography measured in run C1-11 of Bittner (1994) is used to validate the bedform of side bars. The geometry of the channel has been described in 3.1.1, but the computational domain is changed as shown in Figure 3-6a, which consists of a total of 3,192 nodes and 5,460 elements. The zoomed-in element mesh in a cycle of width variation is demonstrated in Figure 3-6b. There are totally 19 cycles included in this domain, the upstream and downstream reaches are extended, where the bed elevations remain fixed. This ensures the conservation of sediment in the channel and that bed evolutions at the upstream and downstream ends would not be affected by unstable flows [Defina, 2003; Zech et al., 2006].

The VA model is used for the computation of flow dynamics. The boundary condition imposed at the upstream is the specified unit discharge $q_0 = 0.0073$ m^2/s. No-penetration condition is used at the sidewalls. Initially, flow depths are all set as 0.022 m, the bed is flat with a slope of 0.004. The helical flow coefficient $a = 3$. The sediment influx is calculated with the flow conditions at the extended upstream reach. The upwind coefficient (ω) used in flow dynamics model and bed evolution model are 0.75 and 0.5, respectively.

The experimental results compared with the linear solution [Wu and Yeh, 2005] and the computed bed topography of side bars are shown in Figure 3-7, the measured

bed deformations have a pile of deposition along the near-wall regions at the widest channel width section of a cycle and V-shape scour at the narrowest section of a cycle, where satisfactory agreement is demonstrated. To further compare the bed deformation patterns at different locations, the cycle-averaged measurements and the computed bed topography at four specified sections of a width-variation cycle are shown in Figure 3-8, where the linear solution and numerical results agree well with the measurements. Both linear solution and numerical computation slightly under predict the depth of scour at 1/4π and 2/4π of the width-variation cycle and slightly over predict the depth of scour at 0/4π and 3/4π of the width-variation cycle. However, the numerical computations are more close to the measured than linear solution.

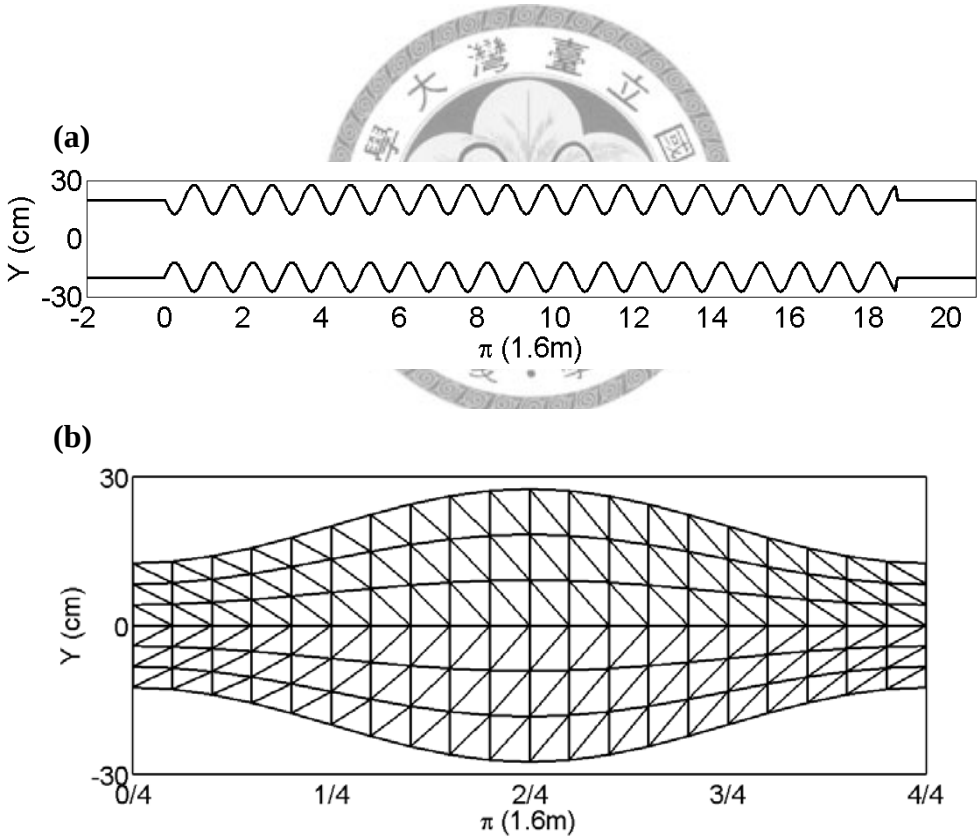

Figure 3-6 (a) Computation domain of Run C1-11 [Bittner, 1994] used in the validation of the bed evolution model; (b) zoomed-in element mesh in a cycle of width variation, the wavelength of cycle (π) is 1.6m

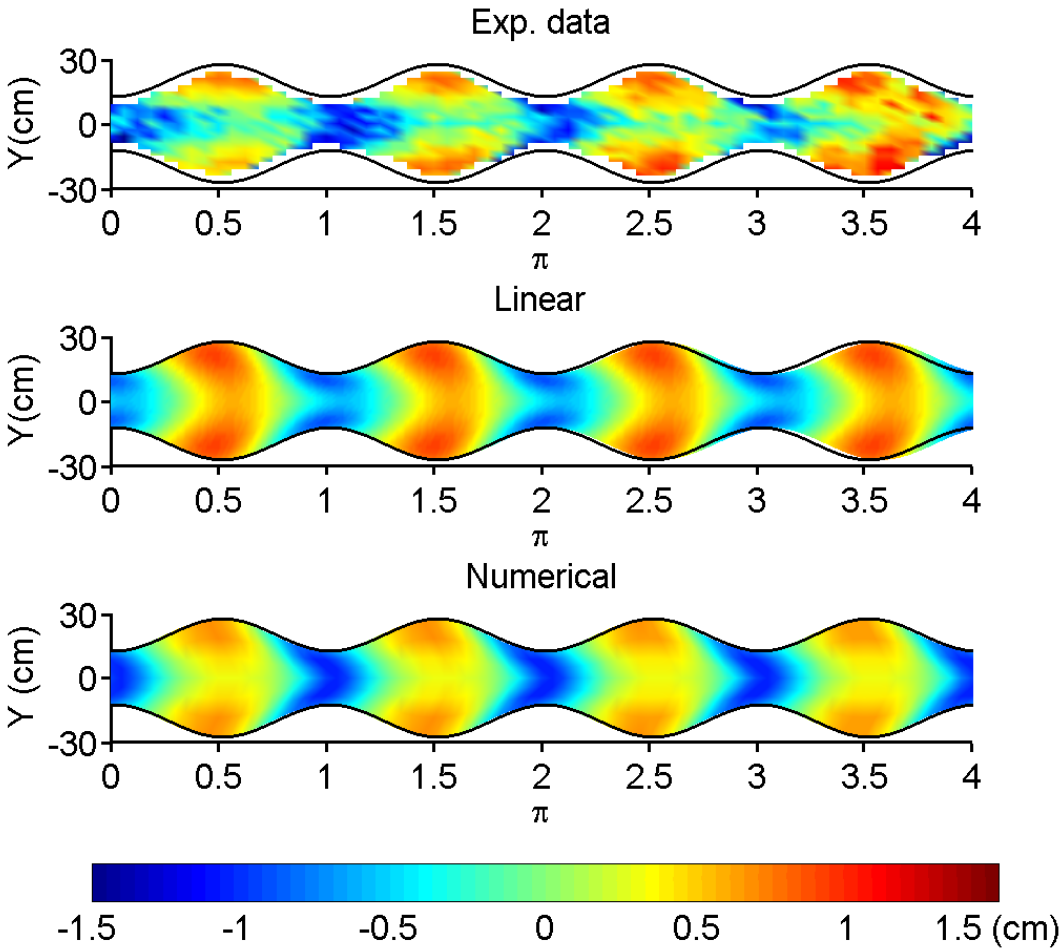

Figure 3-7 Experimental results of Run C1-11 [Bittner, 1994] are compared with the linear solution and computed numerical bed topography of side bars

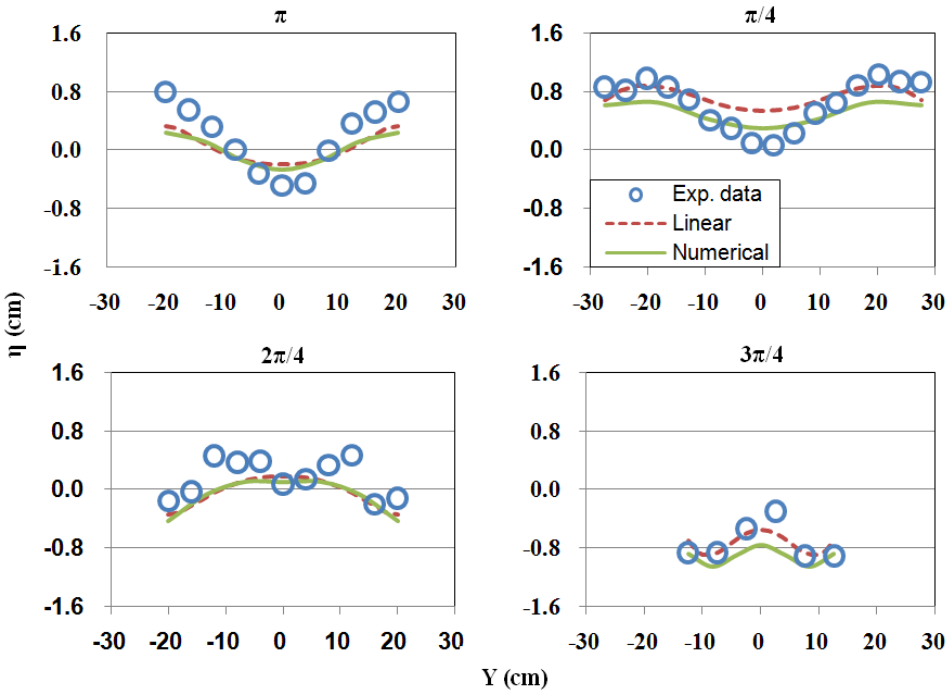

Figure 3-8 Comparison of measured and computed Run C1-11's [Bittner, 1994] results of bed topography at four specified sections of a width-variation cycle

3.2.2 Forced bars – central bars

A series of experiments were conducted in a variable-width channel by Wu and Yeh (2005). One of the experiments, S6, is used here to validate the simulated result of central bars. The sinusoidal variation of the channel width is described by

$$B^* = B_0\left(1 - A\sin\left(\frac{2\pi}{\lambda_c}x\right)\right) \tag{3-2}$$

where B^* is the channel half-width; B_0 is the mean channel half-width whose value was 0.16 m; A is the perturbation amplitude whose value was 0.156; λ_c is the wavelength of the channel whose value was 3.351 m; x is the coordinate in the longitudinal direction. The computational domain is shown in Figure 3-9a, which consists of a total of 2,457 nodes and 4,200 elements. The zoomed-in element mesh in a cycle of width variation is demonstrated in Figure 3-9b. There are totally 6 cycles included in this domain

The VA model is used for flow computations and compared with the result from linear solution. The boundary condition imposed at the upstream is the inflow unit discharge $q_0 =$ 0.0197 m^2/s. No-penetration of water flow is imposed at the sidewalls. The roughness height K_s is 0.004; the helical flow coefficient a is 5. The initial flow depth is given by $D_w = 0.0049$ m, the unit discharge Q_x is set equal to q_0. The initial flat bed has a slope of 0.003. In both the upstream and downstream extended reaches the fixed-bed condition is imposed, the sediment transport rate in the upstream extended reach is used as the sediment influx to the variable-width channel. The upwind coefficient (ω) used in flow dynamics model and bed evolution model are 0.75 and 0.5, respectively.

The computed bed topography of central bars and the experimental result are shown in Figure 3-10, where satisfactory agreement between the experimental and

computed results is demonstrated. The measured central bars have bullet-shape fronts, which are captured more successfully by the linear solution and the numerical models. To further demonstrate this, the lateral bed profiles at the widest and narrowest sections are shown in Figure 3-11. At the widest section of a cycle the linear solution and numerical computation successfully predict the bed elevation in the central region of variation-width channel, but under predict the scour in the near-wall region. At the widest section of a cycle both the linear solution and numerical computation under predict the depth of scour in the central region of variation-width channel, but over predict the scour in the near-wall region. However, the numerical computation model slightly outperforms the linear solution.

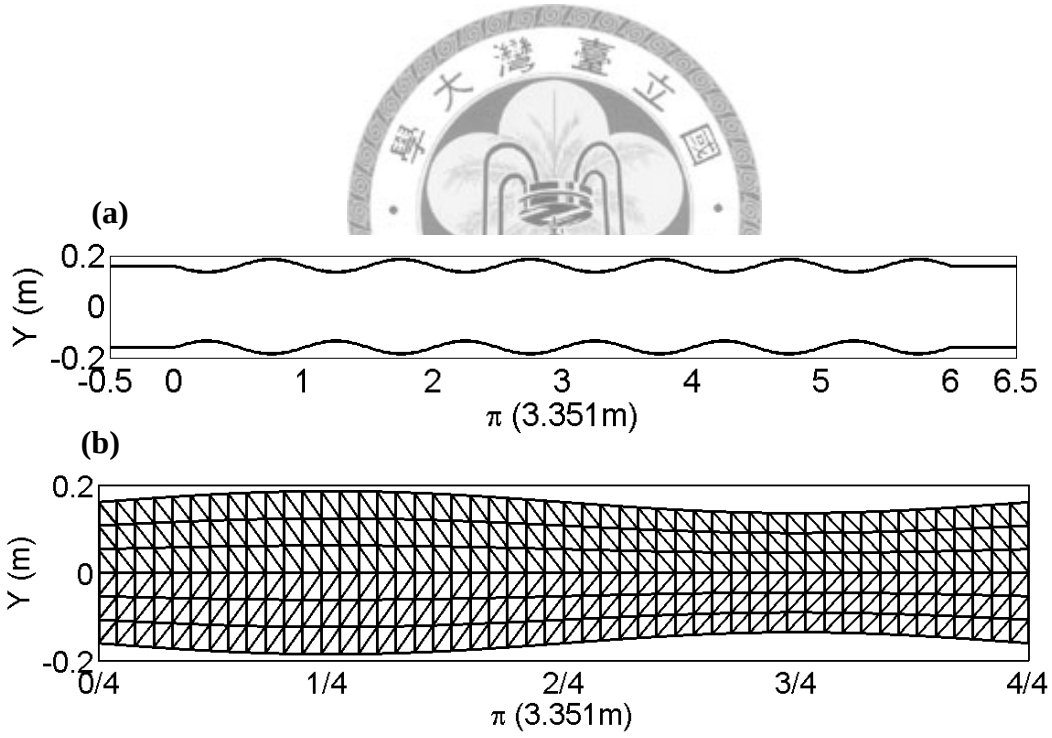

Figure 3-9 (a) Computation domain of Run S6 [Wu and Yeh, 2005] used in the bed evolution model; (b) Zoomed-in element mesh in a cycle of width variation, the wavelength of a cycle is 3.351m

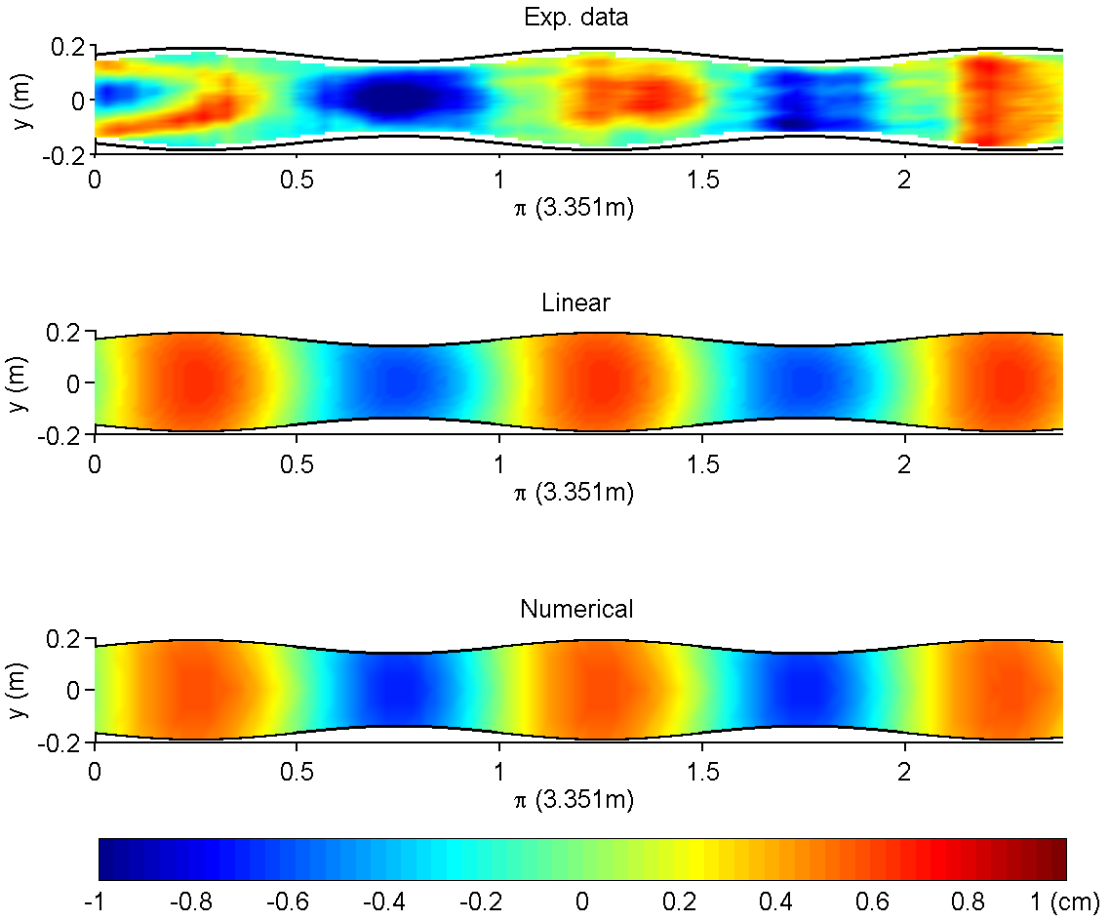

Figure 3-10 Experimental result of Run S6 [Wu and Yeh, 2005] are compared with the linear solution and computed numerical bed topography of central bars

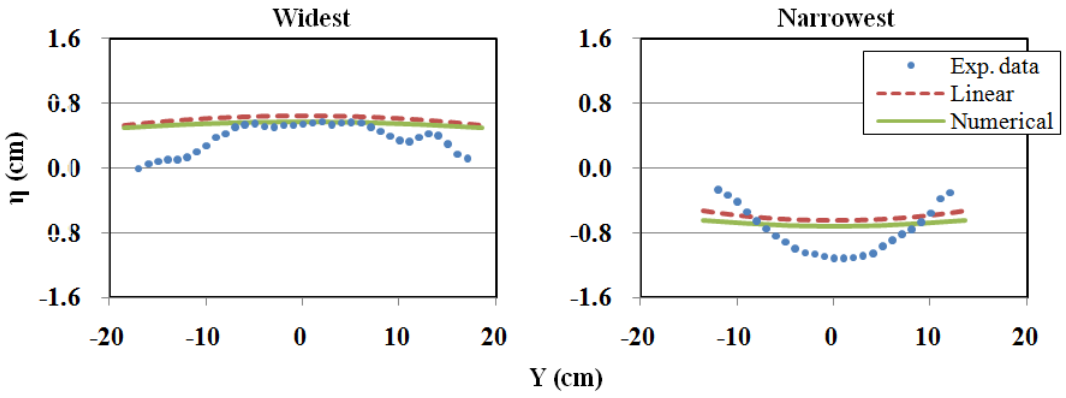

Figure 3-11 Experimental result and computed lateral bed profiles of Run S6 [Wu and Yeh, 2005] at the wide and narrow sections

3.2.3 Free migrating alternate bars

Migrating alternate bars belong to the advection-dominated bed evolution. The traditional Gelerkin method is numerically unstable when used to simulate such cases. Defina (2003) performed a series of numerical experiments on the alternate bars migration using the streamline upwind scheme. In Defina's flow dynamics model, some empirical parameters were used and the sediment transport rate was assumed constant in order to avoid the numerical instability. In our study the CDG scheme is for the first time applied to solve the Exner equation. It is thus of our interest to see if the advection-dominated bed evolution can be simulated reasonably well without degrading the accuracy of sediment transport dynamics.

The numerical simulation performed here follows the numerical experiment of Defina (2003) that is based on the flume experiment of alternate bars conducted by Lanzoni (2000). In the numerical experiment of Defina (2003), an initial disturbance with a single bump was created at the upstream end inducing a train of alternate bars. It should be noted here that even with the same hydraulic condition, different initial disturbances may induce different characteristics of alternate bars in terms of the wavelength, bar height, and celerity. Thus our simulated result of migrating alternate bars is only compared qualitatively with the result of Defina (2003) to validate the bed evolution model.

The parameters used in the numerical simulation are based on the hydraulic condition of the experimental run P1505 [Lanzoni, 2000]. The flume is 1.5 m wide by 55 m long; a length of 120 m is used in the numerical simulation to offer a sufficient space for the alternate bar development. The fixed-bed reaches are extended in both the upstream and downstream of the flume. The computational domain is discretized with a total of 9×481 nodes and 7,680 elements, as shown in Figure 3-12. The initial disturbance is given by the following expression [Defina, 2003] :

$$\delta z_b(x,y) = A_b \cos(\pi y / 2B_0)\sin(2\pi x / \lambda_b) \quad (3\text{-}3)$$

where δz_b = bed disturbance; A_b = perturbation amplitude; B_0 = half-channel width; λ_b = wavelength of bed disturbance. The values of A_b and λ_b are 0.4 cm and 7 m, respectively. Equation (3-3) was used by Defina (2003) to create a single bump that only covered half the channel width, but an initial disturbance covering the whole width (shown in Figure 3-13) is used in this study to accelerate the bar growth.

The VA model is used here for the flow computation. The boundary condition at the upstream is the inflow unit discharge $q_0 = 0.002$ m^2/s. The inflow sediment transport rate is calculated with Equation (2-16) using the hydraulic condition in the extended upstream fixed-bed reach, with the roughness height $K_s = 0.0048$ m. The calculated sediment transport rate is 2.91×10^{-5} m^2/s, which is slightly greater than 2.6×10^{-5} m^2/s measured in the flume. The no-penetration condition is imposed at the sidewalls. The initial bed is flat with a slope of 0.00452. The initial flow depth is assumed equal to 0.044 m; the unit discharge in the x-direction is 0.002 m^2/s; the unit discharge in the y-direction is zero. The upwind coefficient (ω) used in flow dynamics model and bed evolution model are 0.75 and 0.75, respectively.

The simulated evolution of the alternate bars is shown in Figure 3-14. In the first two hours, the initial disturbance migrates downstream and triggers the formation of alternate bars. The upstream alternate bars continue to grow, migrate downstream, and trigger the alternate bars further downstream. After three hours, the diagonal fronts of the alternate bars become more obvious. The bed returns to flat after the train of alternate bars passes by. The bar height, defined as the difference between the extreme elevations in the left and right halves of a cross section, grows with time, as shown in Figure 3-15. The growth rates are steep in the first two hours, and then become mild. The height of the first generated bar, denoted as bar No.1, almost reaches a steady

value after 7 hours. A comparison between the calculated and observed longitudinal profiles of bar height is shown in Figure 3-16. The simulation results are in agreement with the observed bar height and wavelength. The simulated wavelength of the free bars is 12 m, which is slightly greater than 10 m that was observed in the experiment of Lanzoni (2000). The quasi-steady bar height is approximately 6 cm, close to the bar height of 7 cm observed by Lanzoni (2000). The average migration speed is 4 m/hr, greater than 2 and 2.8 m/hr obtained by Defina (2003) and Lanzoni (2000).

The morphodynamic model developed in this study is validated with the forced and free bars. The results indicate that both the linear solution and numerical models would simulate the flowfield reasonably well. However, the numerical model generally outperforms the linear solution. The numerical simulation of free migrating alternate bars reveals that the CDG scheme is applicable to solving the Exner equation.

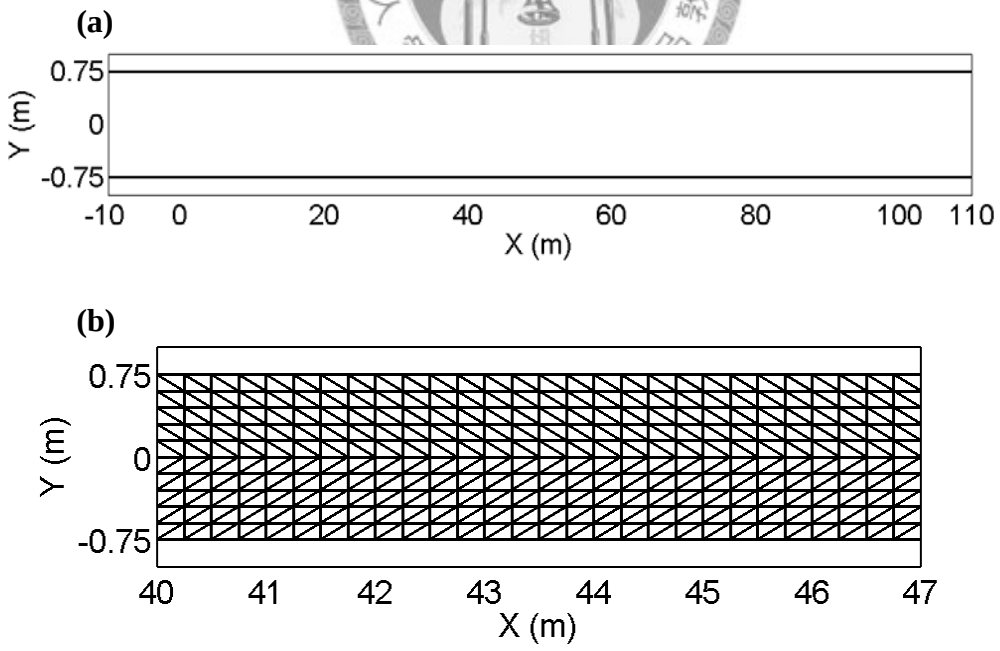

Figure 3-12 (a) Computation domain of Run P1505 [Lanzoni, 2000] used in bed evolution model; (b) zoomed-in element mesh

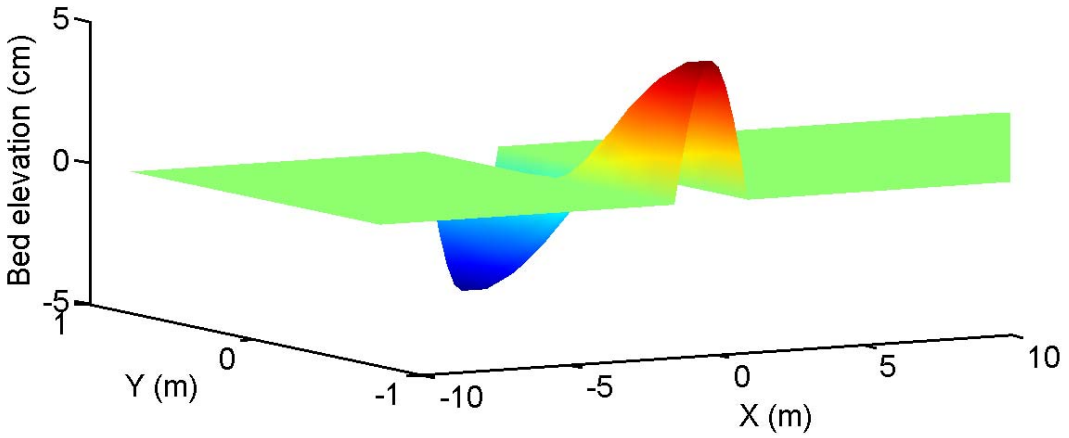

Figure 3-13 Initial disturbance used to trigger the formation of alternate bars in the simulation of Run P1505 [Lanzoni, 2000]

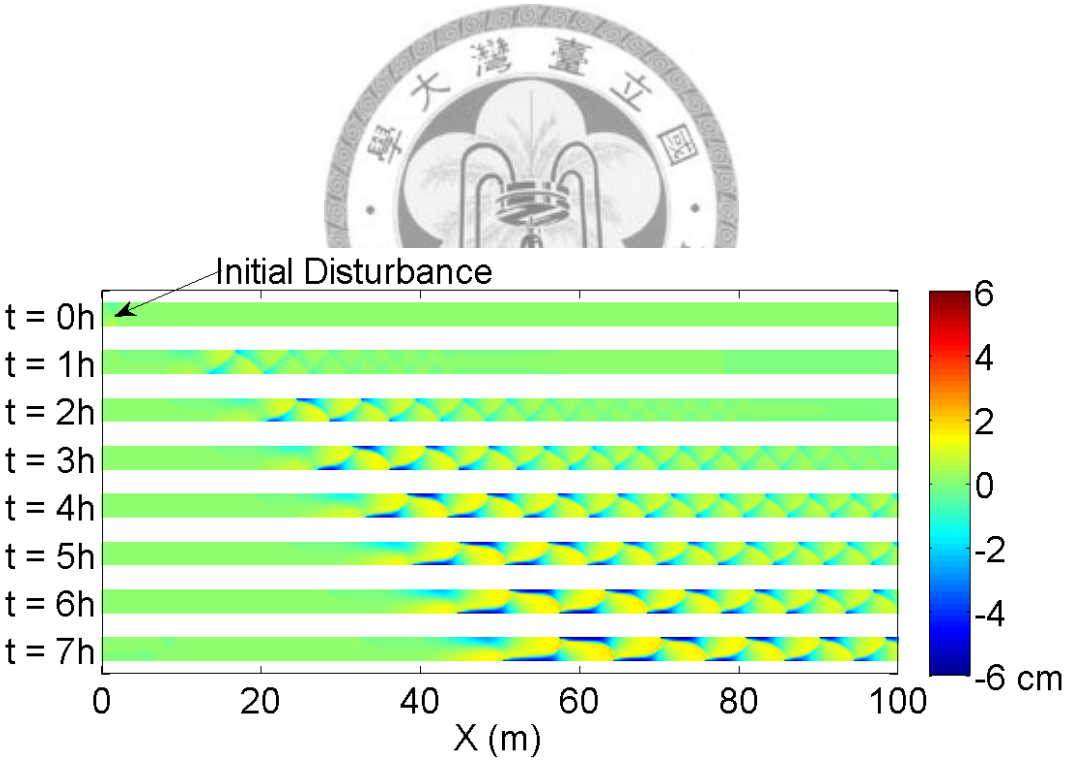

Figure 3-14 Development and migration of alternate bar trains in the simulation of Run P1505 [Lanzoni, 2000]

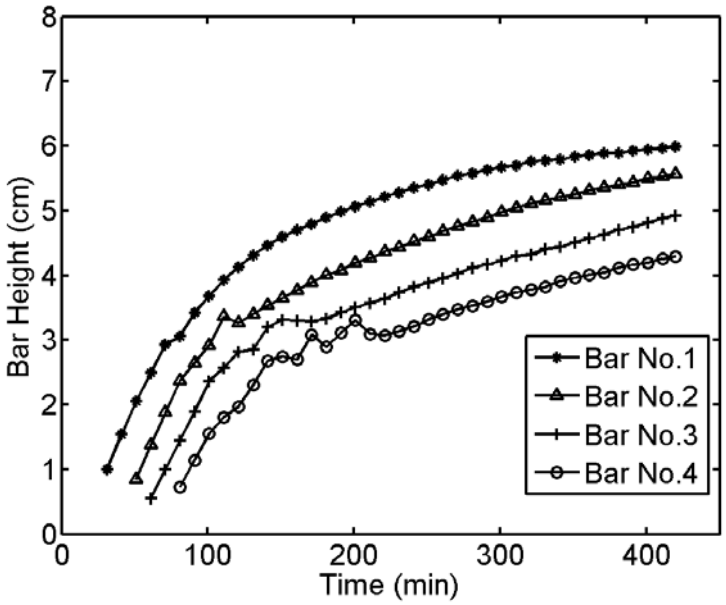

Figure 3-15 Growth of bar height with time in the simulation of Run P1505 [Lanzoni, 2000]. The height of bar No.1 almost reaches a steady value.

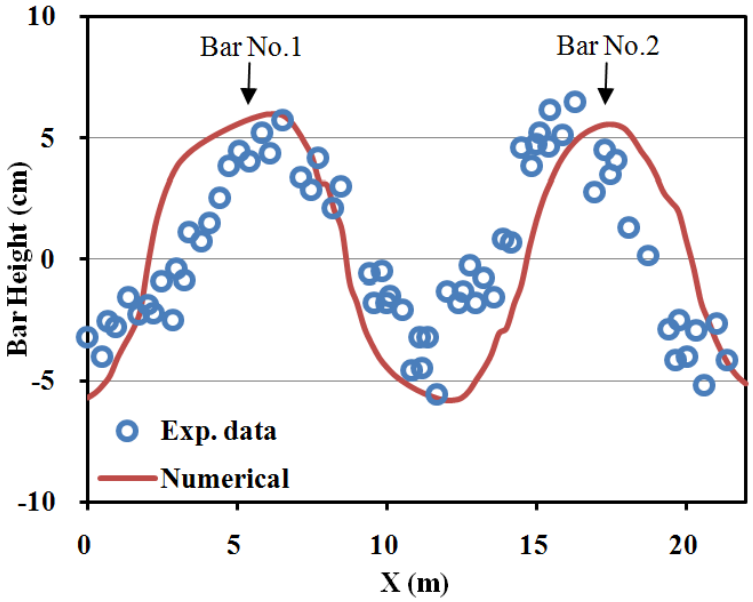

Figure 3-16 Comparison between the calculated and measured Run P1505's [Lanzoni, 2000] longitudinal profiles of bar height. (Bar height is defined as the difference between the extreme elevations in the left and right halves of a cross section.)

3.2.4 Coexistence of free and forced bars

The validated case of coexistence of free and forced bars is chosen from two of a series of experiments conducted in a variable-width channel by Wu and Yeh (2005), labeled as F2 and F7. The experimental bed topography of F2 is central bar paved by an alternative pattern in the channel, as shown in Figure 3-17, thus deduced that the distorted central bar is result of coexistence of free and forced bars. In the experiment of F7, the order of free bars are larger than the force bars, as showed in Figure 3-19, as the results the experimental and simulated topography display a free bars dominated bed forms. The dominated bed deformation of forced bar or free bars in the case of coexistence is attributed to the aspect ratio β [Lanzoni, 2000], which are aspect ratio of F2 and F7 are 5.1 and 13.5, respectively. Higher aspect ratio results in free bars dominated bed forms.

The sinusoidal variation of the channel width is described by Eq. 3-2 with A equal to 0.156 and λ_c equal to 3.35m. The geometry of the channel of F2 and F7 is the same as prescribed in S6 case, and the computation domain is the same as shown in Figure 3-9 which consists of a total of 2,457 nodes and 4,200 elements.

The VA model is used for flow dynamic model. Required computation condition include the roughness height K_s is 0.004, the helical flow coefficient a is 5 and a slope of the initial flat bed is 0.005. The boundary condition imposed at the upstream is the inflow unit discharge (q_0) equal to 0.0137 and 0.005 m^2/s in F2 and F7, respectively. No-penetration of water flow is imposed at the sidewalls. The initial flow depth (D_w) is given by 0.00313 m, the unit discharge Q_x is set equal to q_0. In both the upstream and downstream extended reaches the fixed-bed condition is imposed, the sediment transport rate in the upstream extended reach is used as the sediment influx to the variable-width channel. The upwind coefficient (ω) used in flow dynamics model and bed evolution model are 1.25 and 0.75, respectively.

The computed bed topography and the experimental result of F2 and F7 are shown in Figure 3-17 and 3-19, respectively, where satisfactory agreement between the experimental and computed results is demonstrated. In Figure 3-17 the measured bed topography have distorted bullet-shape fronts, which are similar to central bars superposed by an alternative pattern and are captured more successfully by the numerical models. To further demonstrate this, the comparison of experimental measurement and numerical computation result are made with the lateral bed profiles at four specified sections of a width-variation cycle, as shown in Figure 3-18. The elevation of bed forms are predicted by numerical model exactly. The numerical results agree well with the measurements, except that at 2/4π of the width-variation cycle numerical results under predict the scour depth of the right side of the channel.

In Figure 3-19 the measured bed topography have an alternative scour and deposition pattern, which are similar to free bars are the dominate bed forms in the channels with variable-width and are captured more successfully by the numerical models. The comparison of experimental measurement and numerical computation result are made with the lateral bed profiles at four specified sections of a width-variation cycle, as shown in Figure 3-20, where the computed results agree well with the measurements, except that at 1/4π and 2/4π of the width-variation cycle the model over predicts the deposition of bed elevation.

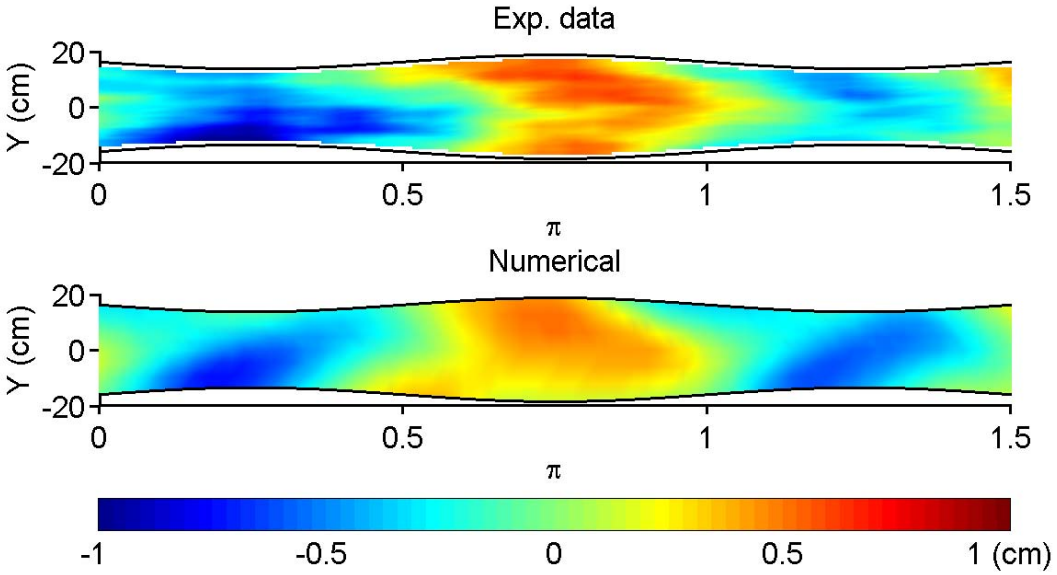

Figure 3-17 Experimental result and computed bed topography of coexistence of forced bar dominated case in Run F2 [Wu and Yeh, 2005].

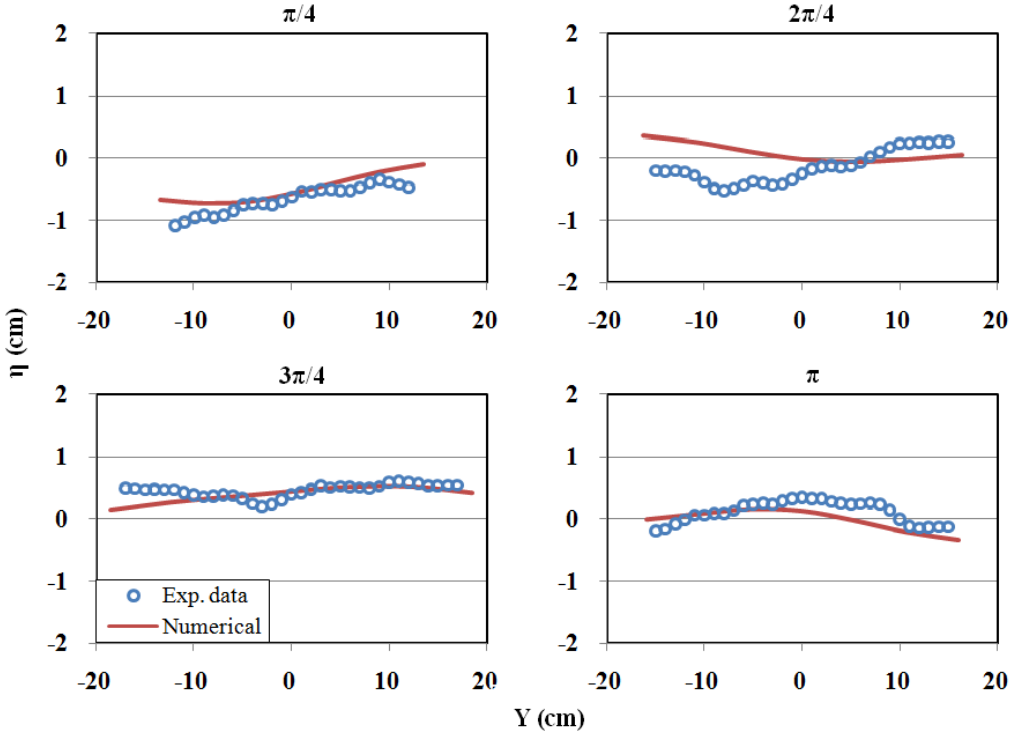

Figure 3-18 Comparison of measured and computed results of bed topography at four specified sections of a width-variation cycle in the case of coexistence of forced bars dominated case in Run F2 [Wu and Yeh, 2005].

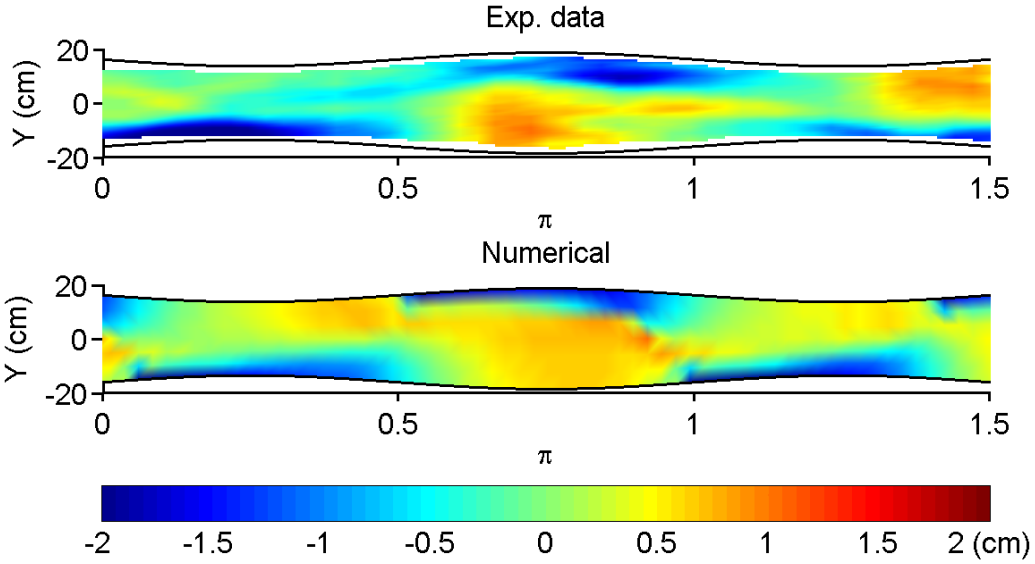

Figure 3-19 Experimental result and computed bed topography of coexistence of free bar dominated case in Run F7 [Wu and Yeh, 2005].

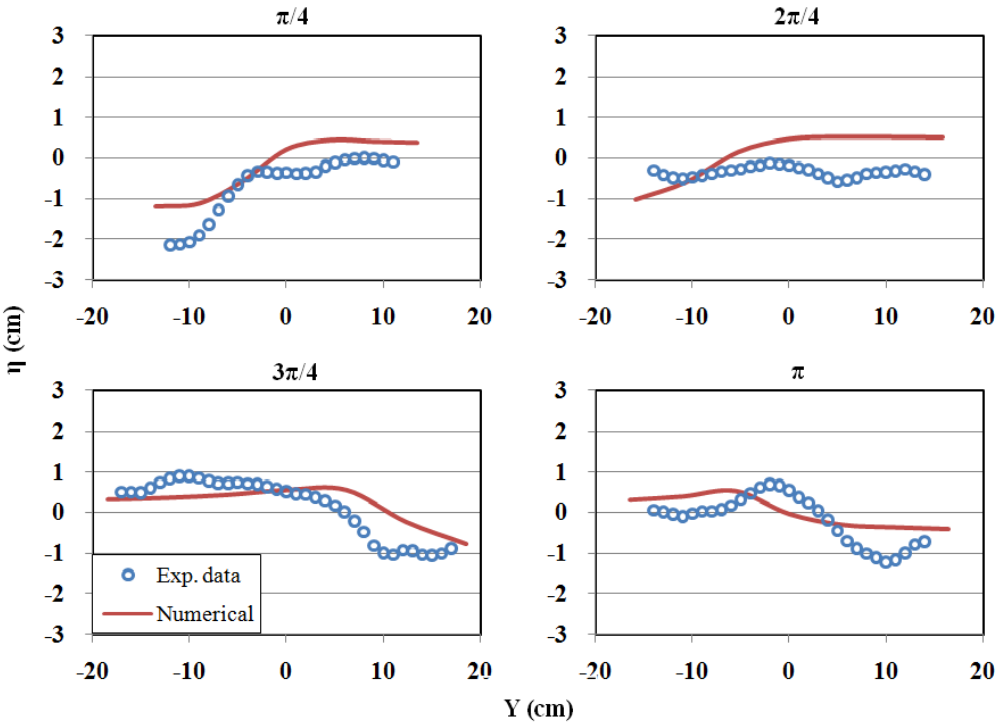

Figure 3-20 Comparison of measured and computed results of bed topography at four specified sections of a width-variation cycle in the case of coexistence of free bars dominated case in Run F7 [Wu and Yeh, 2005].

Chapter 4

Forcing Effect of Width Variation on Free Bars

4.1 Numerical Experiments

A 2D FE morphodynamic model with the VA equation is used to perform the numerical experiments. A series of experiments in which the reference conditions are based on Bernini's numerical experiments [Bernini et al., 2006], named B15 series, were conducted. All conditions remain the same except the channel geometry in each numerical experiment varies. The half-width of the straight channel and mean half-width of the variable-width channel are 0.15 m in B15 series. The wall of the sinusoidal channel was determined by Equation (3-2). Table 4-1 lists the simulation conditions of the numerical experiments. A00W00 represents the reference straight channel, which is used to compare with the variable-width channels.

An upstream disturbance was imposed to trigger the free bars. Prior to imposing the initial disturbance, the bed evolution model was run for sufficiently long time such that equilibrium forced bedform was reached in all channels, as shown in Figure 4-1. The dimensions of the forced bars are proportional to the amplitude of width variation. Most forced bars in B15 series are side bars, except in B15W02 series central bars were observed. Central bars would turn to side bars when the wavelength of the width variation decreases.

A bed disturbance produced by Equation (3-3) was imposed to the upstream extended reach, as shown in Figure 4-2. The width of the upstream extended reach was equal to that of the reference straight channel such that identical disturbances were introduced to all experiments in the same series. The length of the disturbance was 1.6 m, the amplitude was 3 mm. The simulation time was 16 hours.

Table 4-1 Run number and simulation conditions used in B15 numerical experiments

A_c \ λ_b	0.2	0.4	0.6	0.8
0.1	A01W02	A01W04	A01W06	A01W08
0.2	A02W02	A02W04	A02W06	A02W08
0.3	A03W02	A03W04	A03W06	A03W08
0.4	A04W02	A04W04	A04W06	A04W08

A00W00 represent the straight channel (A_c = 0, λ_b = 0)

β	Fr	θ_0	S_0	d_s	q_0
15.0	0.80	0.07	0.005	0.43	0.005

A_c : dimensionless amplitude of width variation

λ_b : dimensionless wave number of width variation

β : ratio of mean half-width to reference flow depth

Fr : Froude number in reference straight channel

θ_0 : dimensionless bed shear stress

S_0 : slope of channel

d_s : grain size [mm]

q_0 : unit discharge [m^2/s]

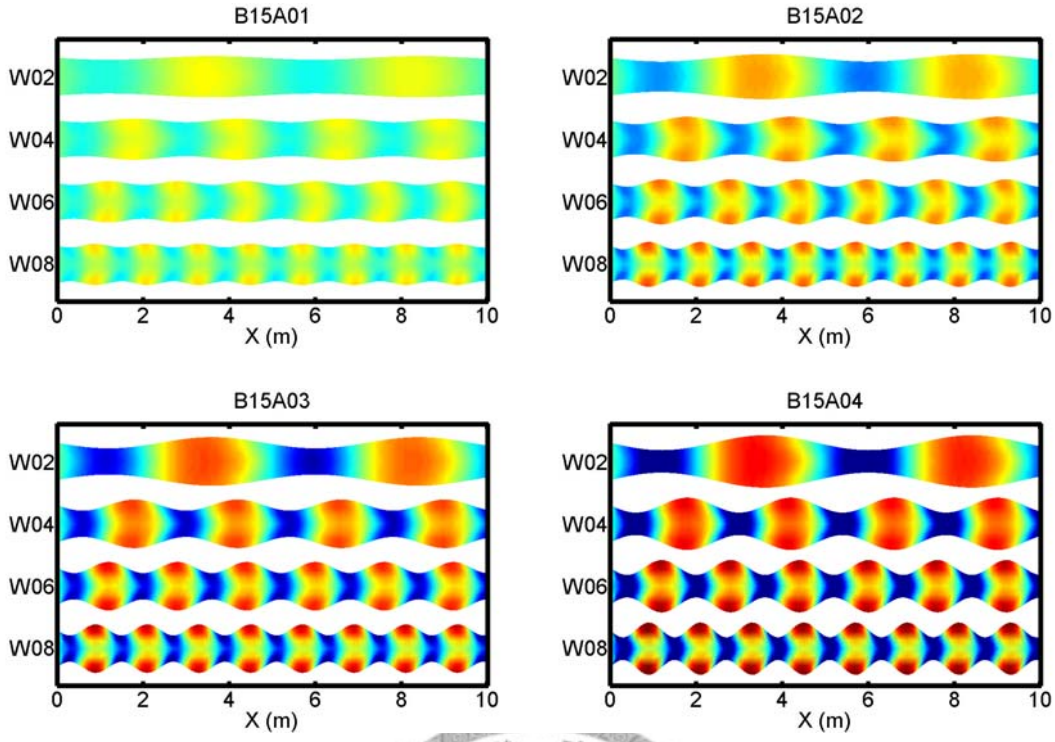

Figure 4-1 Dimensionless bedforms in B15 series. Bedforms are side bars in most cases of B15 series, except in W02 series are central bars. The dimensions of bedforms are proportional to the amplitude of channels with variable-wdith

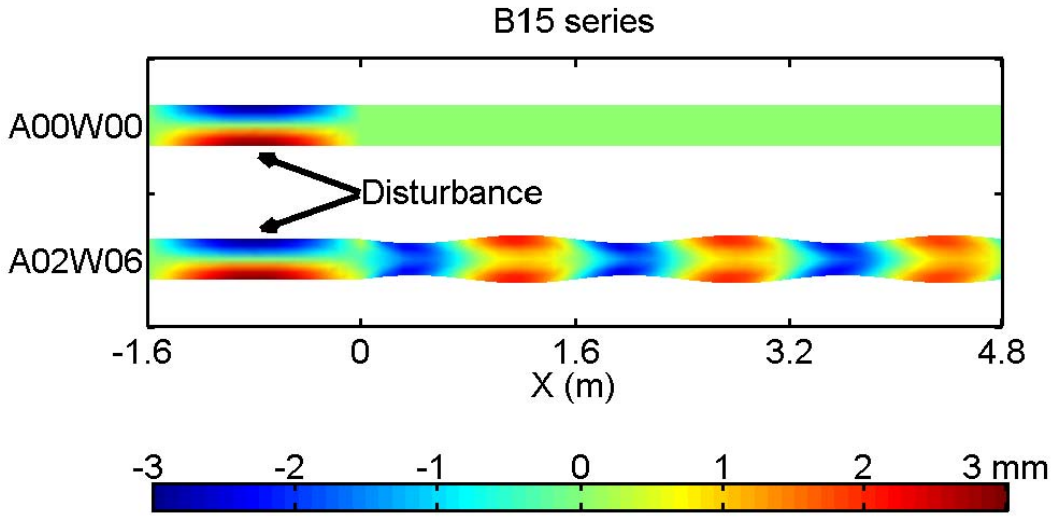

Figure 4-2 A bed disturbance imposed at the upstream extended reach

4.2 Numerical Results

4.2.1 Coexistence of free and forced bars

The coexistence of free and forced bars in the variable-width channels is shown in Figures 4-3(a). In the case of B15A01W06, the height of free bars is much greater than that of forced bars. Numerical simulations revealed that as the train of free bars moved over the forced bars and then migrated downstream, the original characteristics of the forced bars that were left behind would recover.

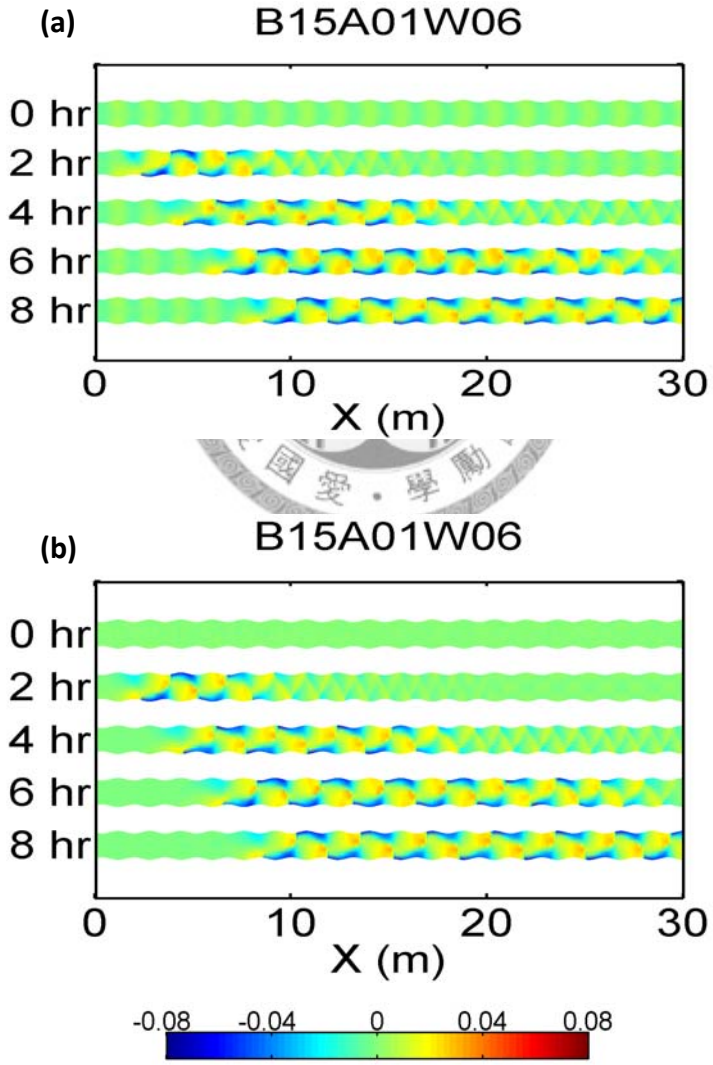

Figure 4-3 In B15A01W06 (a) Coexistence of free and forced bars; (b) Free bar components

The coexistence of free and forced bars gives rise to the nonlinear interactions [Blondeaux and Seminara, 1985; Tubino and Seminara, 1990; Whiting and Dietrich, 1993]. Such interactions may suppress the development of free bars [Kinoshita and Miwa, 1974; Tubino and Seminara, 1990]. To quantify this forcing effect on free bars, the equilibrium forced bar components were subtracted from the mixed free-forced bar patterns (Figure 4-3 (b)). The resulting free-bar components were compared with those forming in the straight channels. The discussions here include the height, wavelength, and celerity of the free bars. The bar height is defined as the difference between the extreme bed elevations in the left and right halves of a cross section, the profile of bar height is shown in Figure 4-4. Downstream of the initial disturbance area, peaks of the bar height profile are labeled as Bar01, Bar02, and so on. The first five peaks were used as the target bars in the present study because they emerged at early stages of the numerical simulations and exhibited sufficient temporal and spatial evolutions. The wavelength is defined as the distance between the negative peaks immediately up- and down-stream of a target bar. These definitions offer an advantage of translating the 3D bar configurations into 2D bar characteristics.

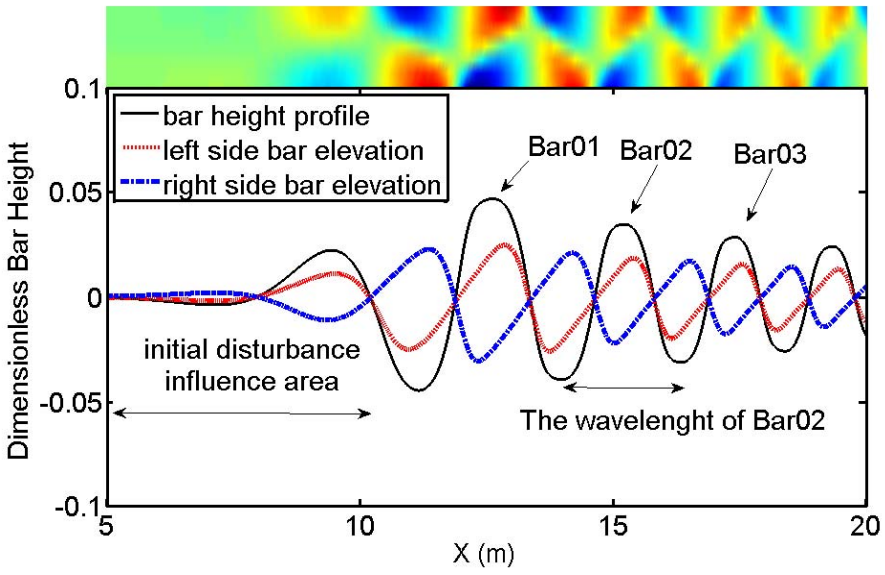

Figure 4-4 Definition sketch of bar height profile

4.2.2 Evolution of free bars in channels with variable width

To investigate the forcing effect of width variation on free bars, the feature of the free bars in the straight channel was first captured as a reference state for comparison. Shown in Figure 4-5 are the free bar component in channels with variable-width. In Figure 4-5(a) the distribution of free bars relate to the wave number of channels with variable width. The peaks of bar height obviously appear in the narrow section of channels and much milder in the wide section. It represents that the variation of channel width have ability to compress and slacken the formation of free bars. Fixed the wave number of channels with variable-width, the deformation of free bars are proportional to the amplitude of channels, as shown in Figure 4-5(b). Observed the free bars patterns at 10m in Figure 4-5(b), the degree of bar height decrease when the amplitude of channels increasing. It implies that amplifying the amplitude of channels result in the suppression of free bars.

The evolution of the characteristic of free bars, ex: the bar height, wave length and celerity, in straight channel (A00W00) reach to the equilibrium stage after 10 hours, as shown in Figure 4-6. The equilibrium bar height, wave length and celerity are 1.18cm, 3.2m and 1.8 cm/min, respectively, which are mostly equal to Bernini's simulation. The bar height reach to the equilibrium stage first, then wave length and celerity achieve. Defina (2003) described the analogous phenomena in her numerical simulation. Evolutions of free bars in the variable-width channels, however, exhibited wavy patterns of bar growth in response to the local variations of channel width. The trends of bar growth in the variable-width channels are similar to those in the straight ones when the forcing effects are small.

To quantify the effect of width variation on free bars, the bar height (B_H) and wavelength (B_L) of the target bars were normalized by the corresponding values in the straight channels such that the ratios represent the relative effect of width variation. Moreover, the evolution is expressed using the number of cycles experienced by the target

bars given that the variation of channel width is periodic. These treatments are used in the subsequent analyses. For example, in Figure 4-7 the bar height of target bar in A02W06 was divided by the same target bar in straight channel, as a result the Y-axis in Figure 4-7 represent the ratio of bar height at the same moment. The location of the target bar can be transformed from the corresponding time axis, thus the X-axis in Figure 4-7 was labeled by the number of cycle. The maximum bar height of target bar in each cycle become convergent when the development of target bars reaches equilibrium. It is worthwhile to mention that shifting the target bar by cycle the equilibrium stage of all target bars will overlap in sequence, just like a resonant. It implies that all target bars in channels with variable-width have the same characteristic in the equilibrium stage.

The train of free bars migrates downstream meanwhile induces new bars further downstream. The induced free bars have characteristics similar to upstream ones and transmit those characteristics to downstream. Shown in Figures 4-8 are the evolutions of bar characteristic ratio as a function of the number of width variation cycles, where the number of cycles experienced by each target bar is shifted such that the resonant stages are all overlapped. In Figure 4-8 (a), for example, all bars in B15A01W06 reached the final resonant stages. The resonant state of Bar01 is the longest, indicating that Bar01 reached the resonant stage first, followed by Bar02, and so on. Variations of the bar height (B_H) and wavelength (B_L) of the free bars are highly related to the wave length of channels with variable-width. The sensitivities of the wavelength and celerity to the forcing effect are, however, different. In Figures 4-8, for example, the bar height ratios range between 0.85~1.15 in A02W02 while in A02W08 range between 0.9~1.0. The variation of bar height ratio is inversely proportional to the wave number of channels with variable-width. There is minimum variation of bar wavelength ratio when the wave number of channels is 0.6 (W06 series). It may be due to that the wave length of free bars in straight channel which is equal to 3.2m, which is twice of the wave length of W06 series (1.6m). The

variation of channel width and wave length of free bars in W06 series are in phase, as a result bar wave length ratio in W06 are nearly equal to unity.

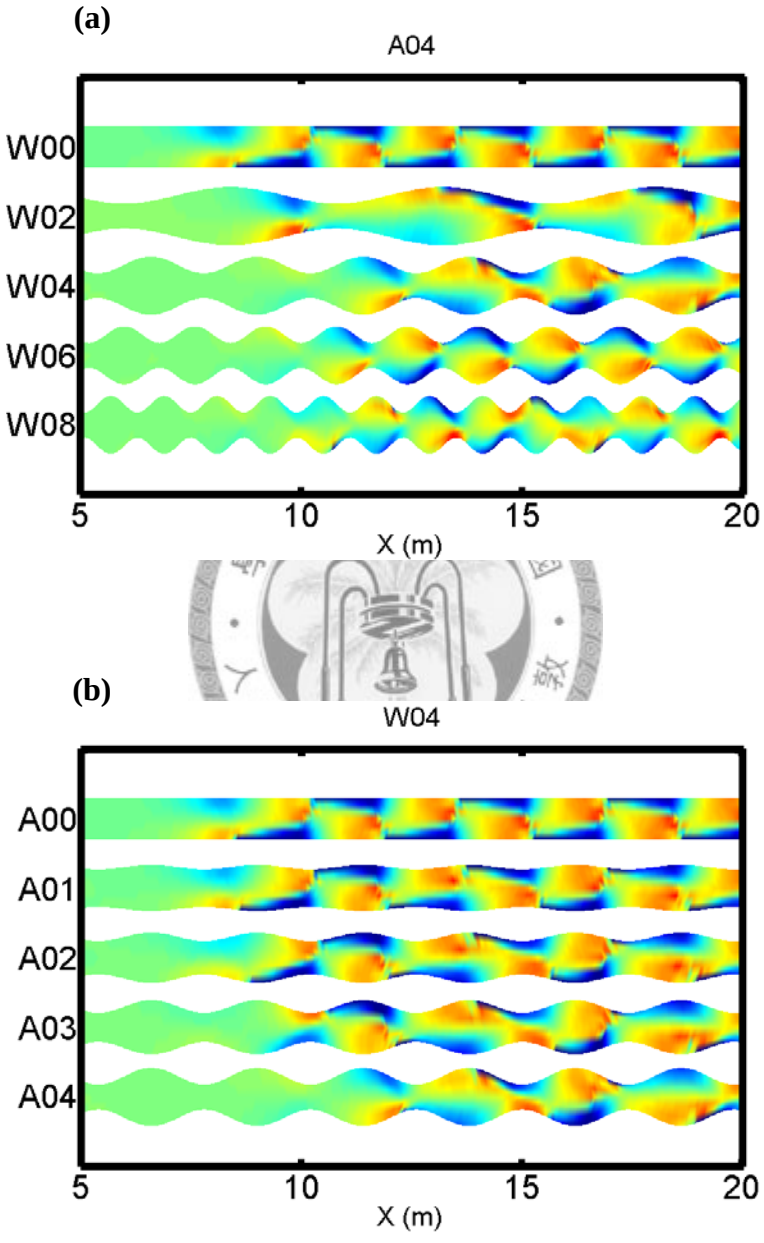

Figure 4-5 Free bar component in (a) A04 which the amplitude of channels is fixed and the wave number is altered and (b) W04 series at 8 hour. W00 and A00 represent the same straight channel run.

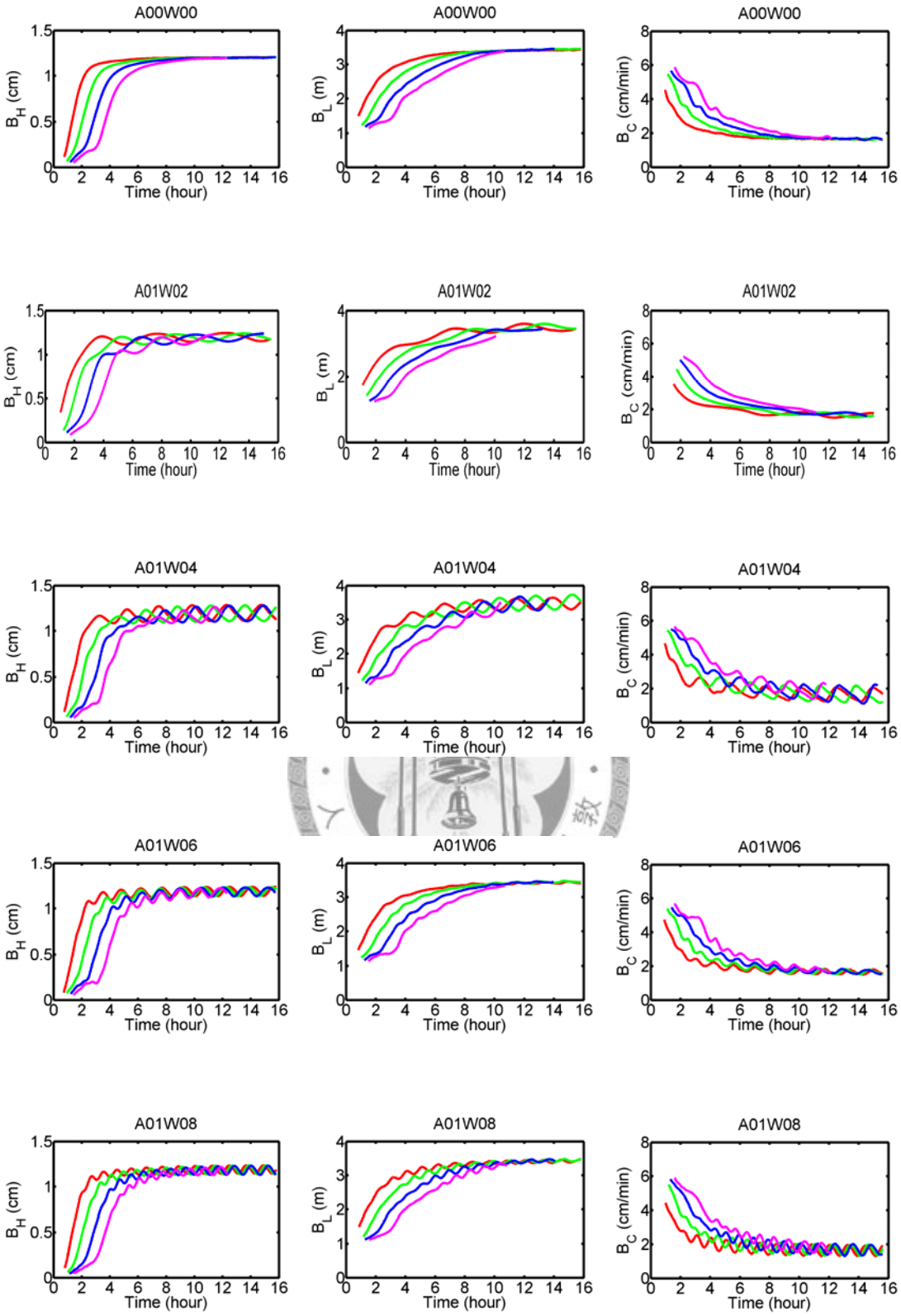

Figure 4-6 Bar height (B_H), celerity (B_C) and wavelength (B_L) evolves with time in B15 series.

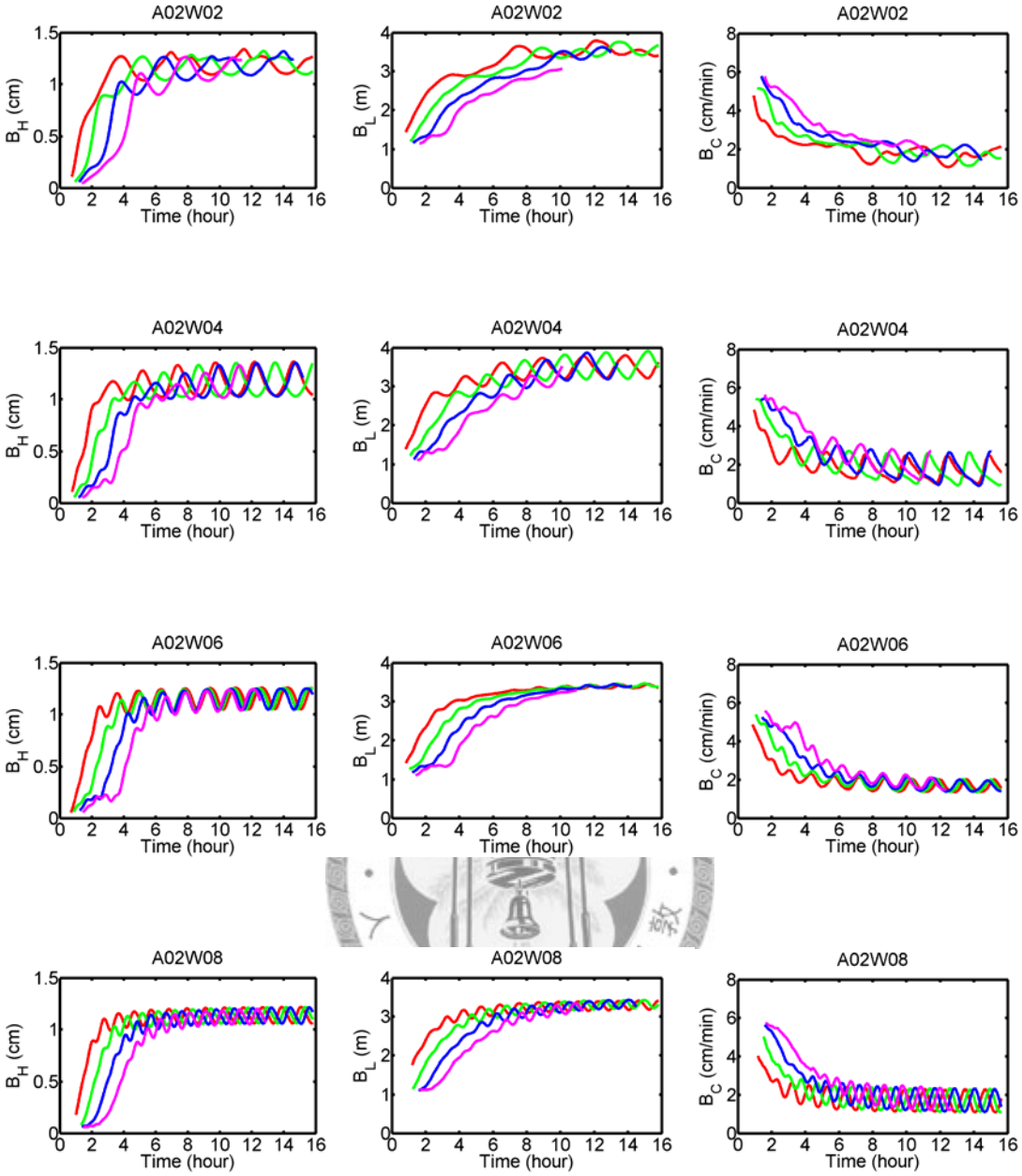

Figure 4-6 (continued)

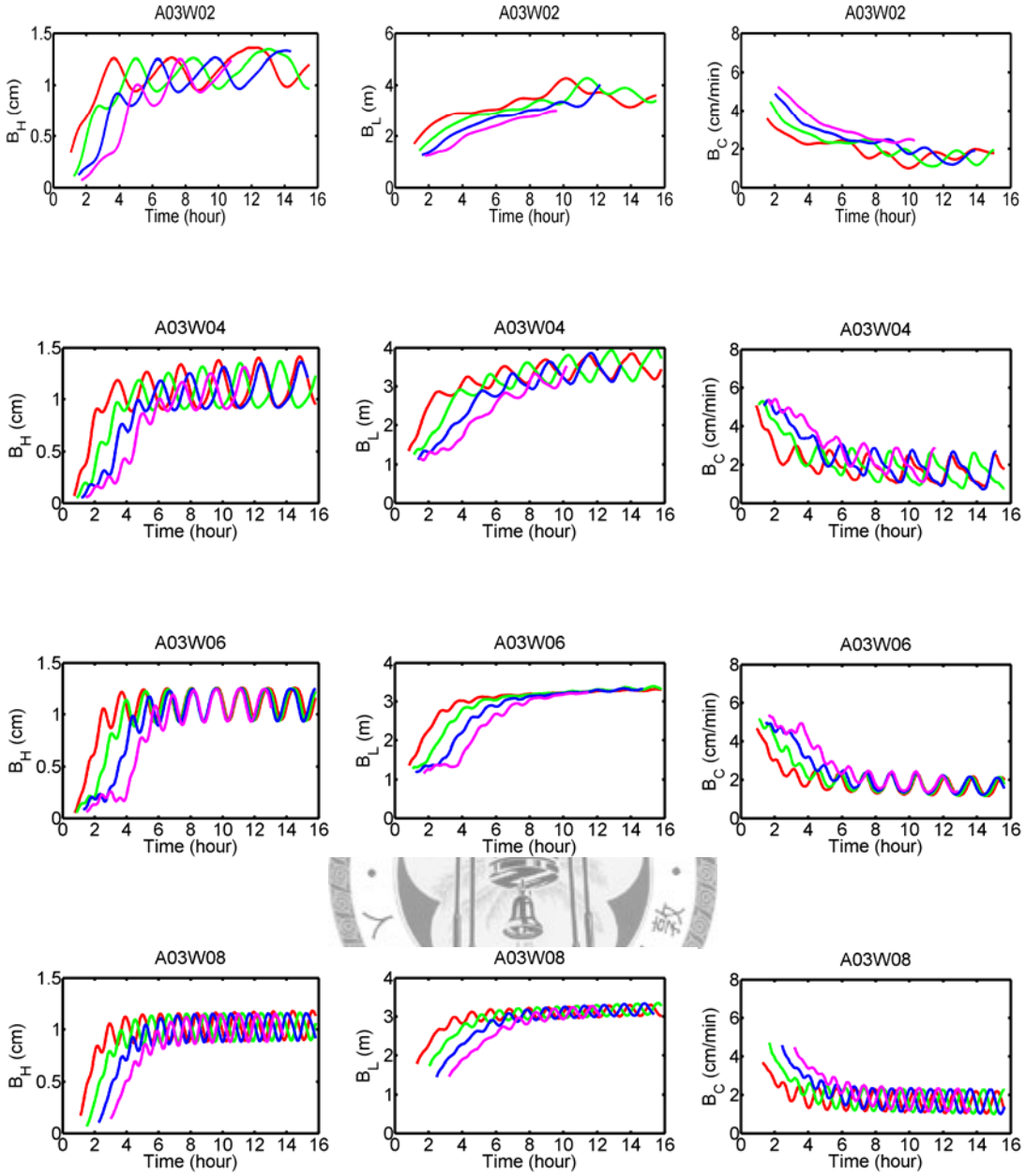

Figure 4-6 (continued)

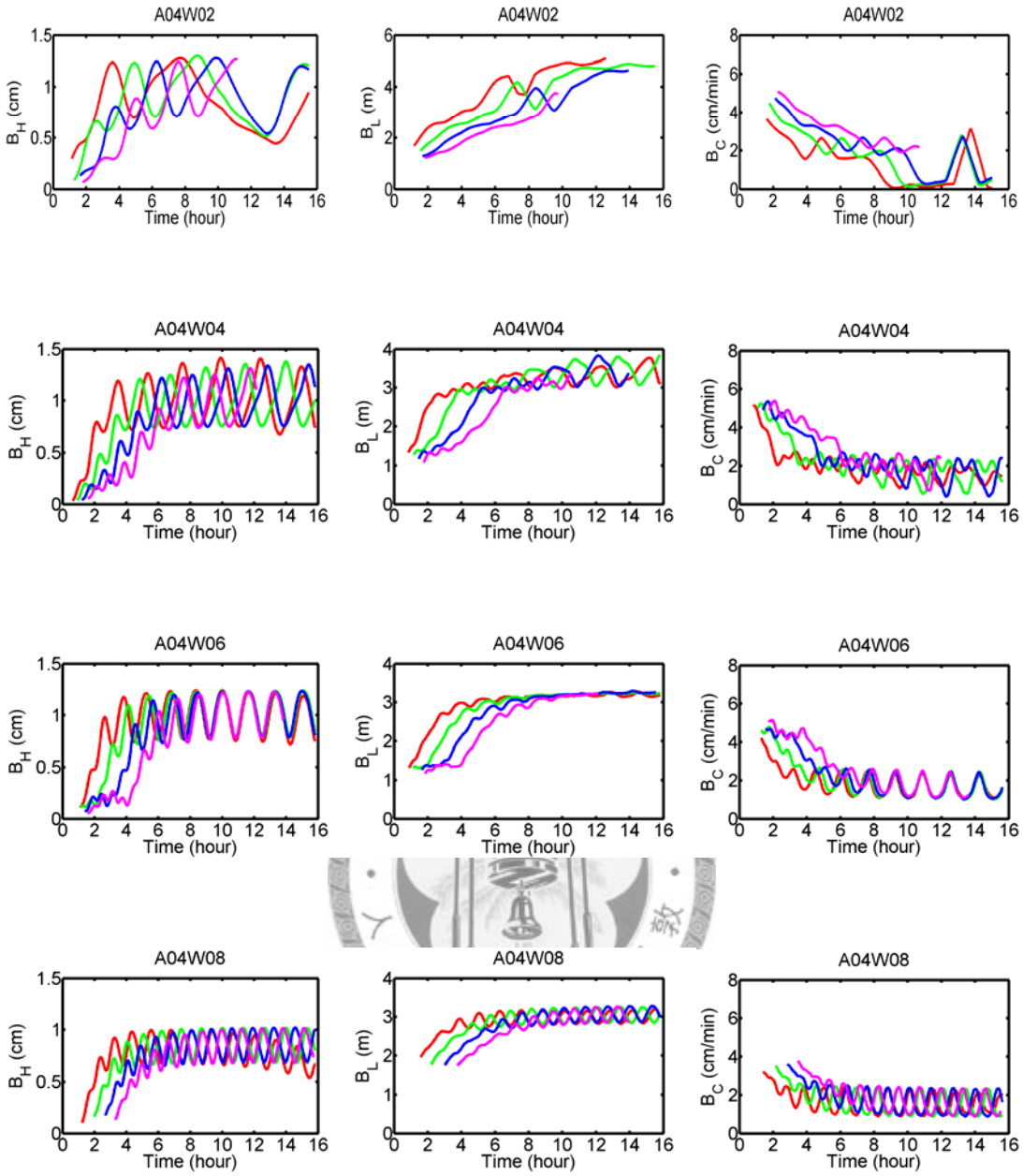

Figure 4-6 (continued)

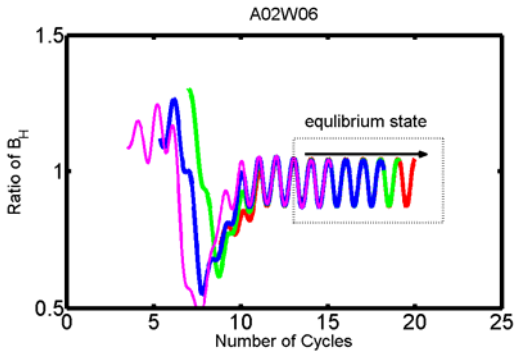

Figure 4-7 Acquire the equilibrium stage of target bars.

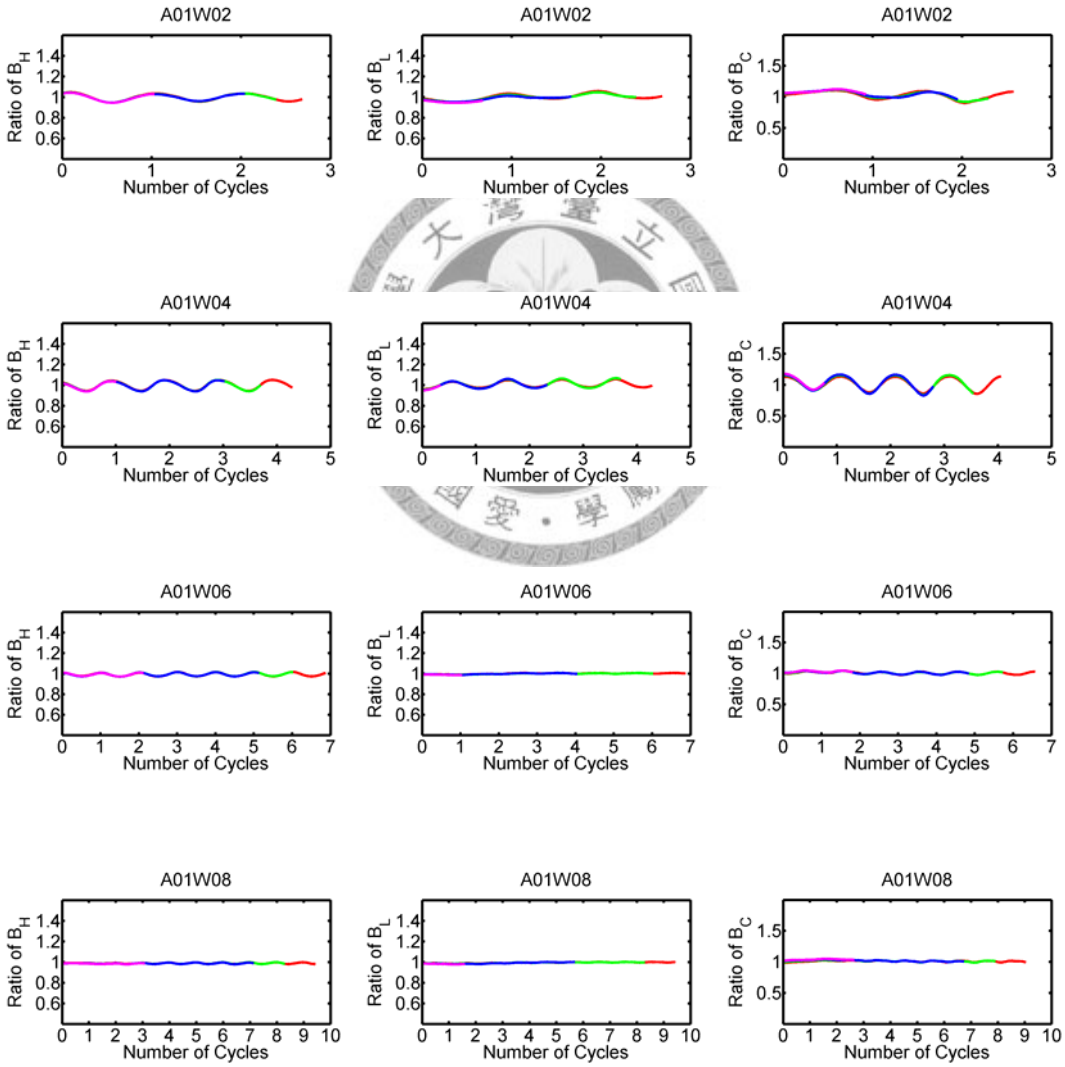

Figure 4-8 Bar height (B_H), wavelength (B_L) and celerity (B_C) reach to the equilibrium state.

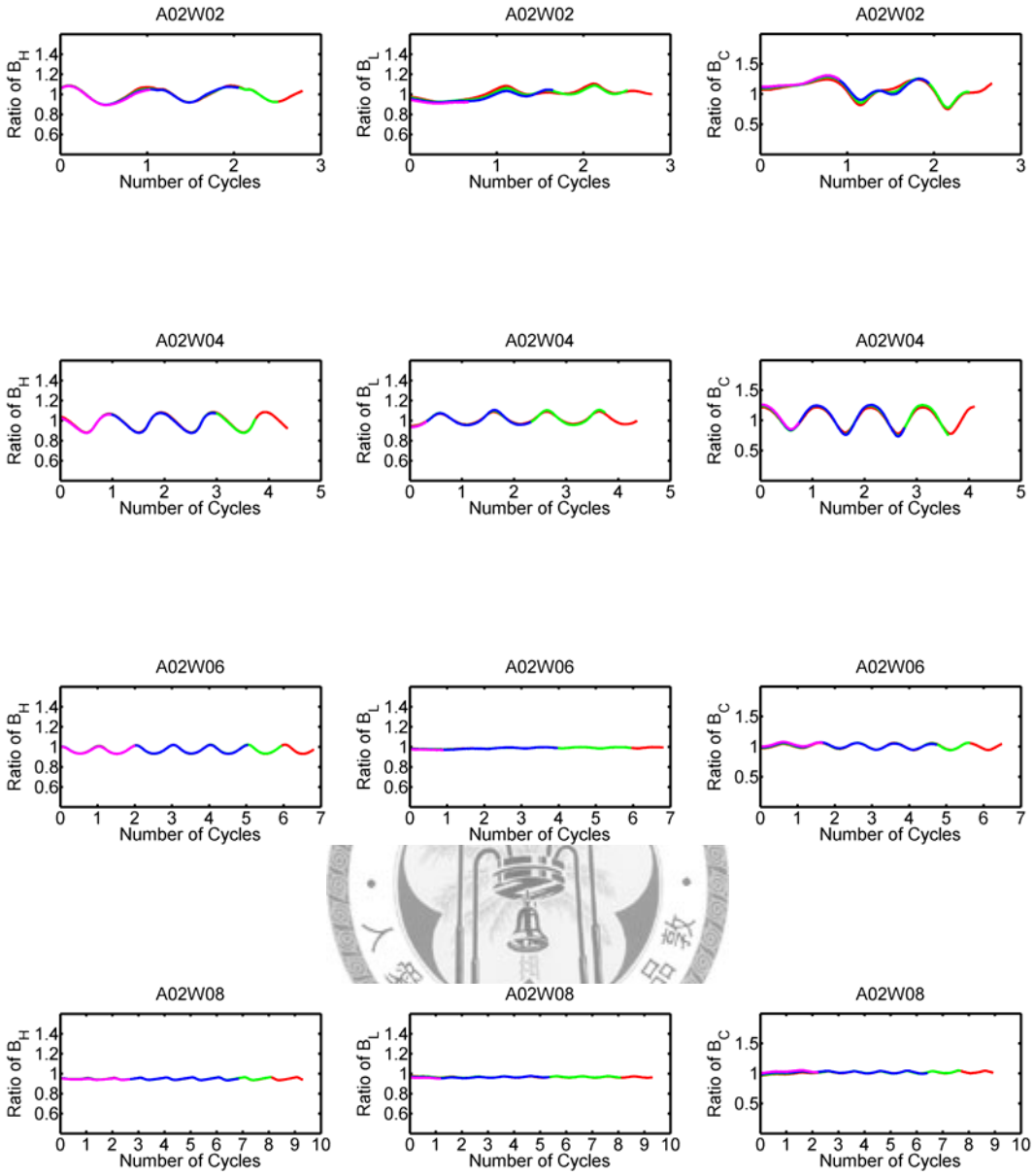

Figure 4-8 (continued)

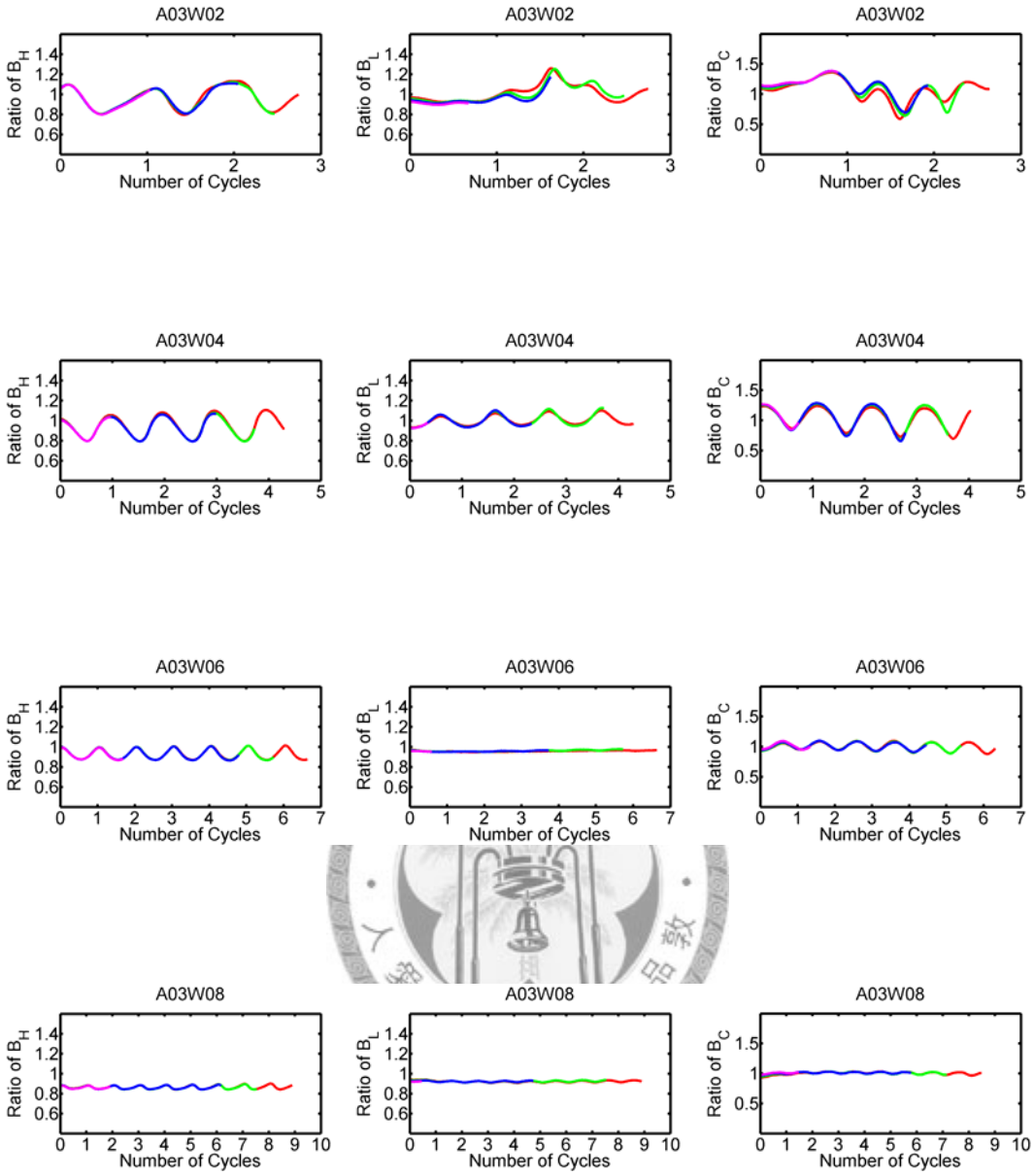

Figure 4-8 (continued)

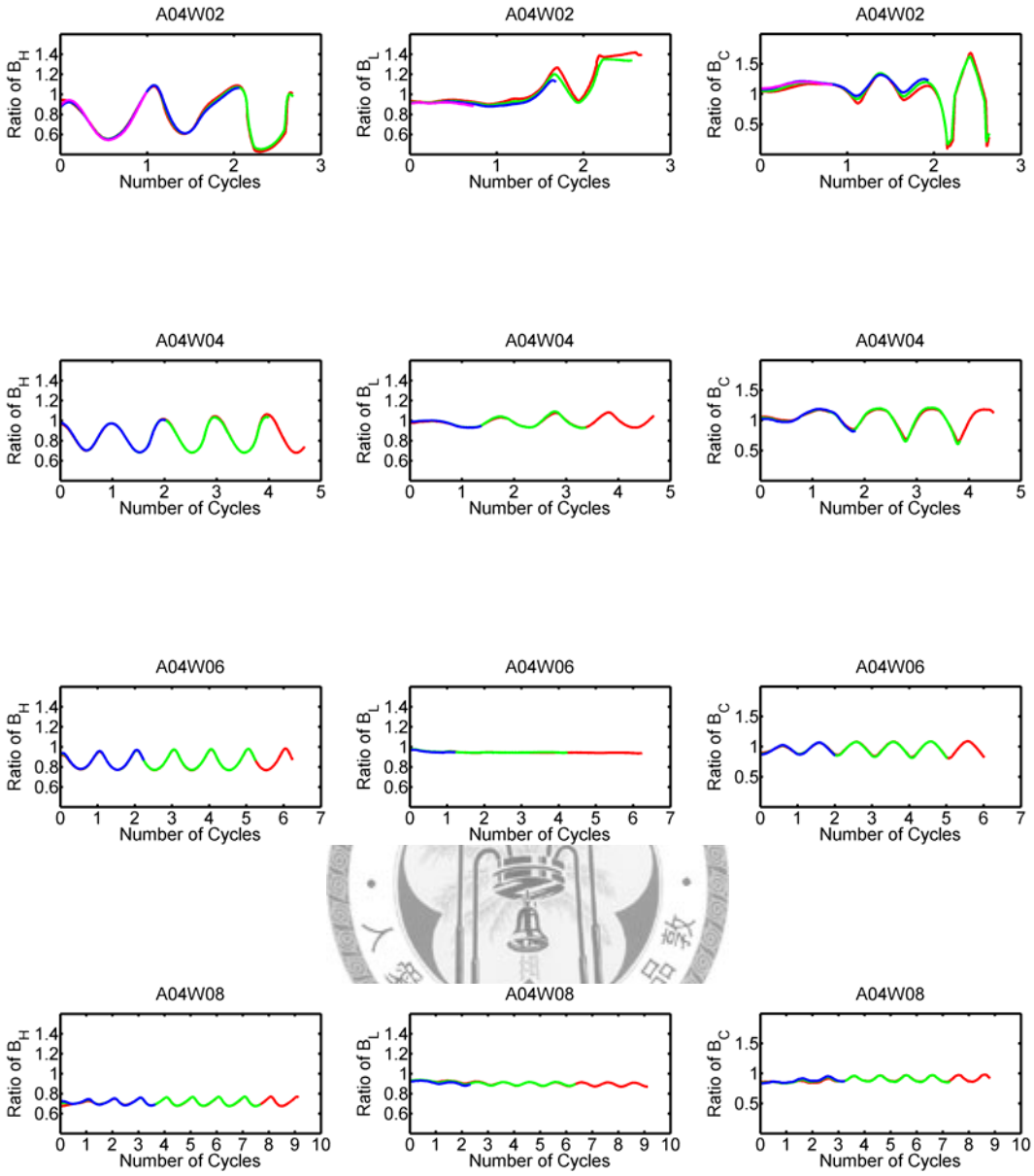

Figure 4-8 (continued)

4.2.3 Quantitative forcing effect on equilibrium stage

The forcing effect of width variation can be quantified using the amplitude and wavelength of the wall sinuosity. The forcing effect of the variable-width channel can be represented by two factors. The first is the wavy factor (WN), defined as the dimensionless wave number of the variable-width channel, representing the waviness frequency of the channel wall. The second is the amplitude factor (Amp), defined as the ratio of amplitude to channel width, representing the degree of width perturbation. Shown in Figure 4-9 are the ratios of equilibrium bar characteristics varying as a function of wavy and amplitude factor, which display a suppression trend. The combination of the wavy factor and amplitude factor defines the forcing factor. The expression of forcing factor FF is taken to be :

$$FF = Amp \times e^{WN} \tag{4-1}$$

The equilibrium bar heights in B15 series are used as the outcomes corresponding to the forcing effect of width variation. The regression relation between the ratios of equilibrium bar height (B_H), wavelength (B_L) and celerity (B_C) and the forcing factor are

$$RB_H = -0.38FF^{2.16} + 1 \tag{4-2a}$$

$$RB_L = -0.13FF^{2.16} + 1 \tag{4-2b}$$

$$RB_C = -0.16FF^{2.16} + 1.041 \tag{4-2c}$$

Figure 4-10 shows a satisfactory coefficient of determination R^2=0.95, 0.93, and 0.87, respectively. The power of the forcing factor is 2.16 in all regression which implies the defined forcing factor is consistent with bar evolution. Figure 4-10 also demonstrates the suppression of free bars by the forcing effect as the equilibrium bar characteristics declines with the increasing forcing factor.

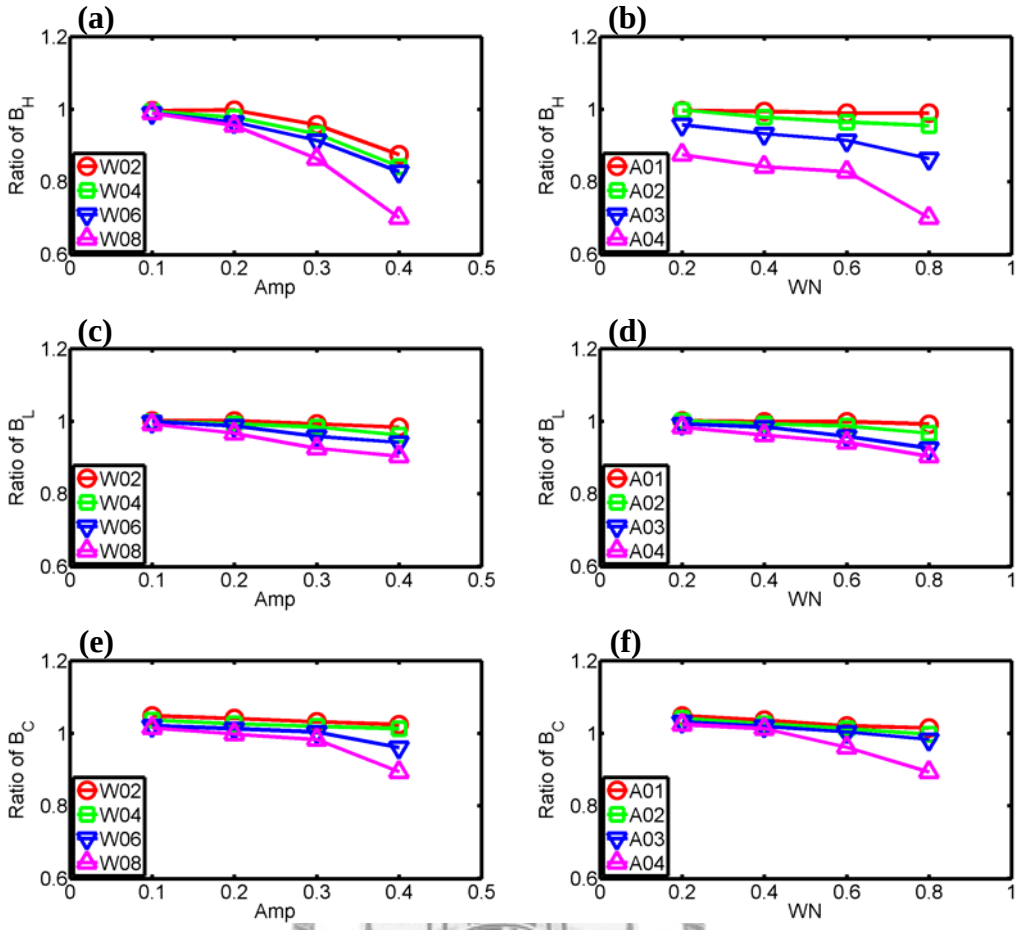

Figure 4-9 Ratio of equilibrium (a) bar height, (c) wavelength and (e) celerity vs. Amp. factor, (b) bar height, (d) wavelength and (f) celerity vs. WN factor.

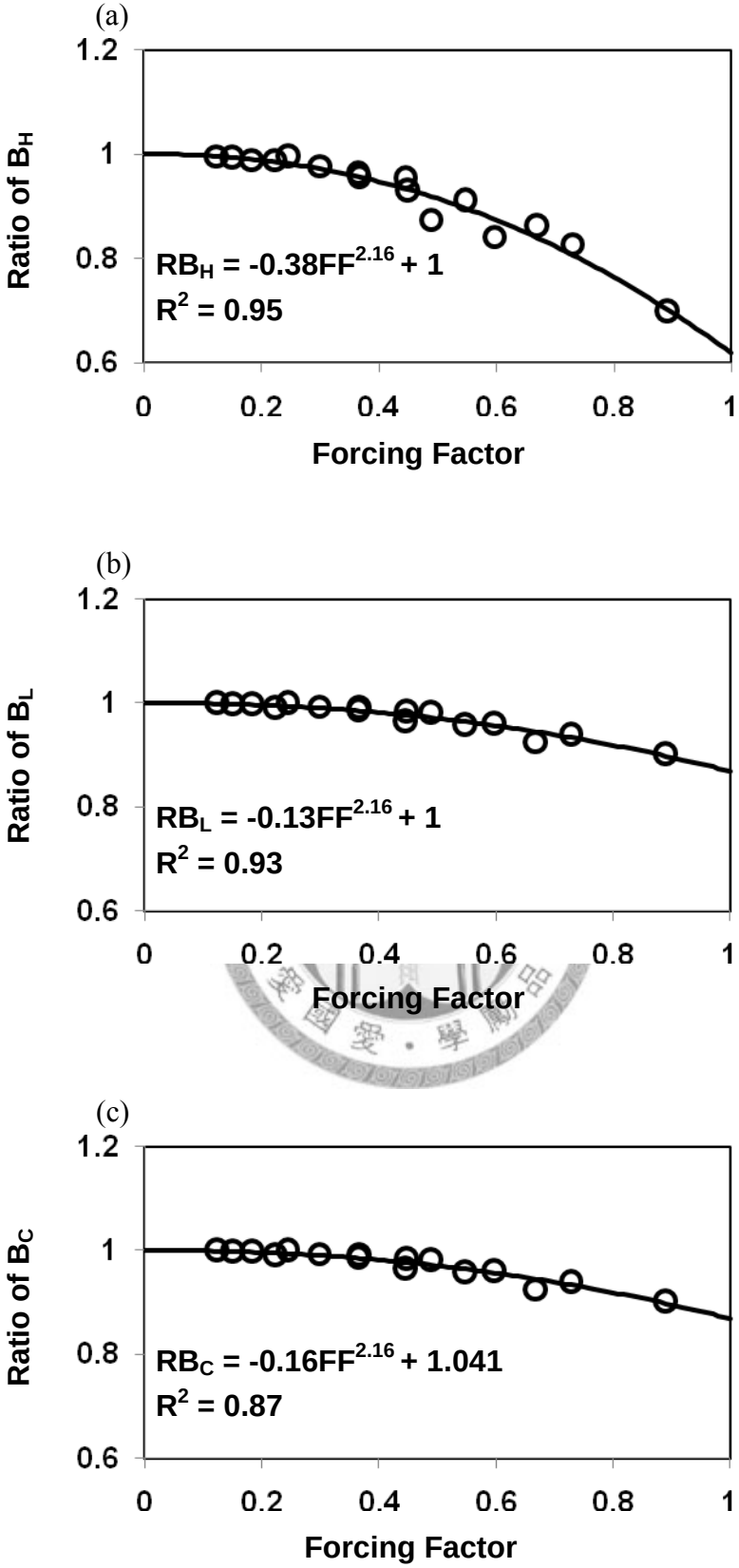

Figure 4-10 Ratio of equilibrium (a) bar height, (b) wavelength and (c) celerity vs. forcing factor

Chapter 5 Conclusions

5.1 Conclusions

5.1.1 2D morphodynamic model

1. A general 2D morphodynamic model was developed here. The most important improvement made in this study is applying the Streamline Upwind Petrov Galerkin (SUPG) scheme to the sediment continuity equation. The resulting bed evolution model has the ability to simulate the translation dominated bedform, such as the free migrating alternate bars.

2. The Vertical Average model (VA) was used in the morphodynamic model and compared with the linear theory of regular perturbation method [Wu and Yeh, 2005]. A comparison between numerical model and linear theory reveals that both of them have similar results, but the numerical model obtained more accurate results in the simulation.

3. We are the first to successfully simulate the evolution of free bars using the FE scheme without degrading the revolution of sediment transport in a unit discrete element, attributable to the application of SUPG scheme in solving the sediment continuity equation. The translation and dispersion of the bedform are captured and validated with the cases of forced bars (side bar and central bar), free bars in straight channel, coexistence of free and forced bar (low and high average aspect ratio) which involve the general cases of bed deformation.

5.1.2 Influences of forcing effect on free bars

1. Numerical simulations revealed that as the train of free bars moved over the forced bars and then migrated downstream, the original characteristics of the forced bars that were left behind would recover. Evolution of free bars will reach an equilibrium state, which are the same as those developing in a straight.

2. The time evolutions of bar characteristic (bar height, wavelength, and celerity) reach a equilibrium state during a sufficient period. Shifting the target bar by cycle the equilibrium stage of all target bars will overlap in sequence, just like a resonant. It is implies that all target bars in channels with variable-width have the same characteristic in equilibrium stage.

3. Evolutions of free bars in the variable-width channels, however, exhibited wavy patterns of bar height, wavelength, and celerity in response to the local variations of channel width. The trends of bar characteristic (height, wavelength, and celerity) in the variable-width channels are similar to those in the straight ones when the forcing effects are small.

4. The variation of bar height ratio is inverse proportion to the wave number of channels with variable-width. There is minimum variation of bar wavelength ratio when the wave number of channels is 0.6 (W06 series). It may be due to that the wave length of free bars in straight channel which is equal to 3.2m is twice of the wave length of W06 series (1.6m). The variation of channel width and wave length of free bars in W06 series are in phase, as the result bar wave length ratio in W06 are nearly equal to unity.

5. The forcing effect of the variable-width channel can be represented by two factors, which are the wavy factor (WN) and the amplitude factor (Amp). the ratio of equilibrium bar characteristics varying as a function of wavy and amplitude factor and display a suppression trend.

6. The expression of forcing factor is defined as: FF = Amp x e^{WN}. The regression relation between the ratio of equilibrium bar height (B_H), wavelength (B_L) and celerity (B_C) and the forcing factor have a satisfactory coefficient of determination R^2=0.95, 0.93, and 0.87, respectively. The free bars suppressed by the forcing effect with the power of 2.16 demonstrate the equilibrium bar characteristics declines with the increasing forcing factor.

5.2 Suggestions

1. The ranges of flow conditions (e.g., average aspect ratio) may be expanded to obtain more general and broadly validated conclusions regarding the influences of forcing effect on free bars.

2. To explain the suppression of free bars in channels with periodic width variations, theoretical models that employ the perturbation [Murdock, 1999] theory may be developed in the future.

3. The channel forcing effects include the width variation and channel curvature. Only the effect of width variation is investigated in this study. The forcing effect of channel curvature on free bars, such as the effect of point bars in river bends on alternate bars, may be included in future work.

References

Bernini A., Caleffi V. and Valiani A., 2006, Numerical modeling of alternate bars in shallow channels, *International Association of Sedimentologists in Braided rivers: process, deposits, ecology and management*, edited by Gregory H. Sambrook Smith et al., Blackwell publishing, Malden

Bittner L.D., 1994, River Bed Response to Channel width Variation, Master Thesis, University of Illinois.

Blanckaert K. and de Vriend H.J., 2003, Nonlinear modeling of mean flow redistribution in curved open channels, *Water Resources Research*, 39(12): 6.1-6.14.

Blanckaert K. and Graf W.H., 2004, Momentum transport in sharp open channel bends, *Journal of Hydraulic Engineering*, 130(3): 186-198.

Blondeaux P. and Seminara G., 1985, Aunified bar-bend theory of river meanders, *Journal of Fluid Mechanics*, 157:449-470

Brooks A.N., and Hughes T.J.R., 1982, Streamline upwind/Petrov-Galerkin formulations for convection dominated flows with particular emphasis on the incompressible Navier-Stokes equations, *Computer Methods in Applied Mechanics and Engineering*, 32, 199-259.

Callander R.A., 1969, Instability and river channels. *Journal of Fluid Mechanics*, 36:165-480

Colombini M., Seminara G. and Tubino M., 1987, Finite-amplitude alternate bars, *Journal of Fluid Mechanics*, 181:213-232

Colombini M. and Tubino M, 1991, Finite-amplitude free bars : A fully nonlinear spectral solution, *in Sand Transport in Rivers, Estuaries and the sea*, 163-169, edited by Soulsby R. and Bettes R., published by Balkema A.A. and Brookfield Vt.

Cui Y., Parker G., and Paola C., 1996, Numerical simulation of aggradation and downstream fining, *Journal of Hydraulic Research*, 34(2): 185-204.

Cui Y., and Parker G., 2003a, Sediment pulses in mountain rivers: 1. Experiments, *Water Resources Research*, 39(9), 1239.

Cui Y., and Parker G., 2003b, Sediment pulses in mountain rivers: 2. Comparison between experiments and numerical predictions, *Water Resources Research*, 39(9), 1240.

Defina A., 2003, Numerical experiments on bar growth, *Water Resources Research*, 39(4) : ESG 2

de Vriend H.J., 1976, A mathematical model of steady flow in curved shallow channels, *Journal of Hydraulic Research*, 18(4): 327-341.

Engelund F., 1974, Flow and bed topography in channel bends, *Journal of Hydraulic Division*, 100: 1631-1648.

Engelund F. and Skovgaard O., 1973, On the origin of meandering and braiding in alluvial streams. *Journal of Fluid Mechanics*, 57:289-302

Fredsoe J.,1978, Meandering and braiding of rivers. *Journal of Fluid Mechanics*, 84:609-624

Fujita T. and Muramoto T., 1985, Studies on the process of development of alternate bars, *Bull. Disaster Prev. Res. Inst. Kyoto Univ.*, 35 : 55-86

Fukuoka S., 1989, Finite amplitude development of alternate bars. *in River Meandering, Water Resources Monograph*, 12:237-266, edited by Ikeda S. and Parker G., AGU, Washington D.C.

Garcia M. and Nino Y., 1993, Dynamics of sediment bars in straight and meandering channels : Experiments on the Resonance Phenomenon, *Journal of Hydraulic Researches*, 31(6) : 739-761

Ghamry H.K., 1999, Two dimensional vertically averaged and moment equations for shallow free surface flows, PhD thesis, University of Alberta, Canada.

Ghamry H.K., and Steffler P.M., 2002, Two dimensional vertically averaged and moment equation for rapidly varied flows, *Journal of Hydraulic Research*, 40(5): 579-587.

Ghamry H.K., and Steffler P.M., 2005, Two dimensional depth averaged modeling of flow in curved open channel, *Journal of Hydraulic Research*, 43(1): 44-55.

Giraldo F.X., 1995, A space marching adaptive remeshing technique applied to the 3D Euler equations for supersonic flow, PhD thesis, University of Virginia.

Hicks F.E., and Steffler P.M., 1992, Characteristic dissipative Galerkin scheme for open-channel flow, *Journal of Hydraulic Engineering*, 118(2): 337-352.

Hoger A., and Carlson D.E., 1984, Determination of the stretch and rotation in the polar decomposition of the deformation gradient, *Quarterly of Applied Mathematics*, 42(1): 113-117.

Hughes T.J.R. and Mallet M., 1986, A new finite element formation for computational fluid dynamics: III. The generalized streamline operator for multidimensional advective-diffusive systems. *Computational Methods in Applied Mechanics and Engineering*, 58(3): 305-328.

Ikeda S., Parker G., and Sawai K., 1981, Bend theory of river meanders. Part 1. Linear development, *Journal of Fluid Mechanisms*, 112: 363-377.

Kassem A.A. and Chaudhry M.H., 2002, Numerical modeling of bed evolution in channel bends. *Journal of Hydraulic Engineering*, 128(5): 507-514.

Kinoshita R. and Miwa H., 1974, River channel formation which prevents downstream translation of transverse bars, *Shinsabo*, 94 : 12-17 (in Japanese)

Koch F.G., and Flokstra C., 1981, Bed level computations for curved alluvial channels. *Proceedings of the XIX Congress of the IARH*, New Delhi, India, **2**: 357-388.

Lanzoni S., 2000, Experiment s on bar formation in a straight flume: 1. Uniform sediment, *Water Resource Research*, 36:3337-3349

Lanzoni S. and Tubino M., 2001, Experimental observations on bar development in cohesionless channels, *Excerpta*, G.N.I., 14:119-152, CUEN-Napoli, Napoli, Italy

Lisle T.E., Pizzuto J.E., Ikeda H., Iseya F., and Kodama Y., 1997, Evolution of a sediment wave in an experimental channel, *Water Resources Research*, 33(8): 1971-1981.

Lisle T.E., Cui Y., Parker G., Pizzuto J.E., and Dodd A.M., 2001, The dominance of dispersion in the evolution of bed material waves in gravel-bed rivers, *Earth Surface Processes and Landforms*, 26, 1409-1420.

Molls T., and Chaudhry H.M., 1995, Depth-averaged open-channel flow model, *Journal of Hydraulic Engineering*, 121(6): 453-465.

Murdock J.A., 1999, Perturbations : Theory and Methods, Wiley, NewYork.

Nelson J.M. and Smith J.D., 1989, Flow in meandering channels with natural topography, *in River Meandering, Water Resources Monograph*, 12:69-102, edited by Ikeda S. and Parker G., AGU, Washington D.C.

Parker G., 1976, On the cause and characteristic scales of meandering and braiding in rivers, *Journal of Fluid Mechanics*, 76:457-480

Parker G. and Johannesson H., 1989, Observations of several recent theories of resonance and overdeepening in meandering channels. *In River Meandering, Water Resources Monography*, 12:379-415, edited by Ikeda S. and Perker G., AGU, Washington D.C.

Repetto R., Tubino M. and Paola C., 2002, Planimetric Instability of Channels with Variable Width , *Journal of Fluid Mechanics*, 457: 79-109

Schielen R., Doelman A. and de Swart H.E., 1993, On the nonlinear dynamics of free bars in straight channels, *Journal of Fluid Mechanics*, 252:325-356

Seminara G. and Tubino M., 1989, Alternate bars and meandering : Free, forced and mixed interactions, *in River Meandering, Water Resources Monography*, 12:267:320, edited by Ikeda S. and Parker G., AGU, Washington D.C.

Seminara G., 2006, Meanders, *Journal of Fluid Mechanisms*, 554: 217-297

Shimizu Y. and Itakura T., 1989, Calculation of bed variation in alluvial channels, *Journal of Hydraulic Engineering*, 115(3): 367-384.

Shimizu Y. Tamaguchi H. and Itakura T., 1990, Three-dimensional computation of flow and bed deformation. *Journal of Hydraulic Engineering*, 116(9): 1090-1108

Struiksma N., 1985, Prediction of 2-D bed topography model for rivers. *River Meandering, Water Resources Monograph*, edited by Ikeda S. and Parker G. et al., 8: 151-180, AGU, Washington D.C.

Struiksma N., Olesen K.W., Flokstra C. and De Veriend H.J., 1985, Bed deformation in curved alluvial channels, *Journal of Hydraulic Research*, 23: 57-79.

Tubino M. and Seminara G., 1990, Free-forced interactions in developing meanders and suppression of free bars, *Journal of Fluid Mechanics*, 214 : 131-159

Tubino M., Repetto R. and Zolezzi G., 2000, Free bars in Rivers, *Journal of hydraulic Research*, 37(6) : 759 – 775

Vasquez J.A., 2005, Two-dimensional finite element river morphology model, PhD thesis, University of British Columbia, Canada.

Vasquez J.A., Millar R.G., and Steffler P.M., 2007, Two-dimensional finite element river morphology model, *Canada Journal of Civil Engineering*, 34: 752-760.

Whiting P.J. and Dietrich W.E., 1993, Experimental Constraints on Bar Migration Through Bends: Implications for Meander Wavelength Selection, *Water Resources Research*, 29(4) : 1091-1102

Wu F.C., and Yeh T.H., 2005, Forced bars induced by variations of channel width: Implications for incipient bifurcation, *Journal of Geophysical Research*, 110, F02009

Zech Y., Soares-Frazao S., Spinewine B., Bellal M., and Savary C., 2005, The morphodynamics of super- and transcritical flow, in *River*, *Coastal and Estuarine Morphodynamics*, edited by Parker G. and Garcia M., pp.239-251, Taylor & Francis Group, London.